THE ROLE OF SENSITIVITY MATRIX FORMULATION ON DAMAGE DETECTION VIA EIT IN NON-PLANAR CFRP LAMINATES WITH SURFACE-MOUNTED ELECTRODES
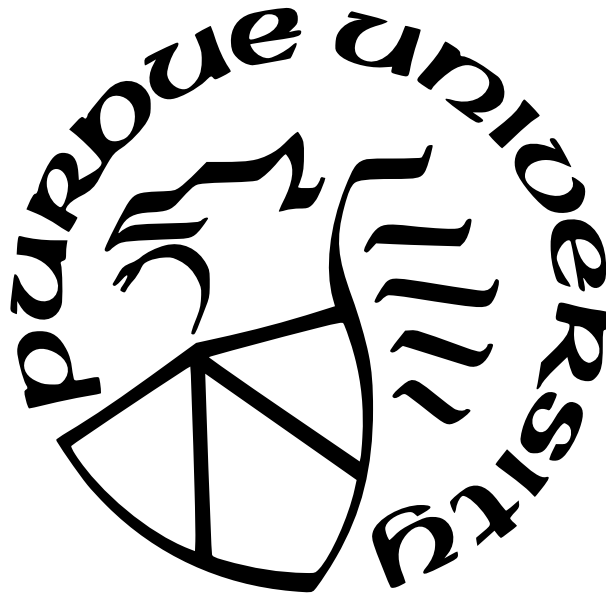
by

Monica S Ashok Sannamani

A Thesis

Submitted to the Faculty of Purdue University

In Partial Fulfillment of the Requirements for the degree of

Master of Science in Aeronautics and Astronautics

School of Aeronautics and Astronautics

West Lafayette, Indiana

August 2021

THE PURDUE UNIVERSITY GRADUATE SCHOOL
STATEMENT OF COMMITTEE APPROVAL

Dr. Tyler N. Tallman, Chair

School of Aeronautics and Astronautics

Dr. Fabio Semperlotti

School of Mechanical Engineering

Dr. Vikas Tomar

School of Aeronautics and Astronautics

Approved by:

Dr. Gregory A. Blaisdell

For Mumma and Dadda

ACKNOWLEDGMENTS

Firstly, I would like to thank Dr. Tyler Tallman. I am grateful to have had him as my advisor. His positive outlook and excellent guidance throughout my graduate studies have hugely contributed to my academic achievements as well as my practical skills as an engineer.

I thank Dr. Semperlotti and Dr. Tomar for being part of my defense committee and taking the time to offer their perspectives.

I would also like to thank Professor Wayne Chen and his student, Jinling Gao for assisting me with optical microscopy.

I sincerely thank my fellow lab mates for always being there to help me out. I truly appreciate all the advice and support I received over the past year and a half. You have been such great friends to me.

My sincere gratitude to my cousins, Pooja and Prarthana, for being my family away from home. To my best friends from undergrad, thank you for always being there for me. Last but not least, I'd like to thank my parents for always cheering me on in my endeavours. I would not have been able to do it without you.

TABLE OF CONTENTS

LIST OF FIGURES

ABBREVIATIONS

BVID   barely visible impact damage

CFRP   carbon fibre reinforced polymer

DC   direct current

EIT   electrical impedance tomography

FOBG   fibre optic bragg grating

GF   glass fibre

NDT   non-destructive testing

SHM   structural health monitoring

SVD   singular value decomposition

ABSTRACT

Carbon fibre reinforced polymers (CFRPs) are extensively used in aerospace, automotive and other weight-conscious applications for their high strength-to-weight ratio. Utilization of these lightweight materials unfortunately also involves dealing with damages unlike those seen in traditional monolithic materials. This includes invisible, below-the-surface damages such as matrix cracking, delaminations, fibre breakage, etc. that are difficult to spot outwardly in their early stages. Robust methods of damage detection and health monitoring are hence important. With the intention of avoiding weight addition to the structure to monitor its usability, it would be desirable to utilize an inherent property of these materials, such as its electrical conductivity, as an indicator of damage to render the material as self-sensing. To this end, electrical impedance tomography (EIT) has been explored for damage detection and health monitoring in self-sensing materials due to its ability to spatially localize damage via non-invasive electrical measurements.

Presently, EIT has been applied mainly to materials possessing lesser electrical anisotropy than is encountered in CFRPs (e.g. nanofiller-modified polymers and cements), with experimental setups involving electrodes placed at the edges of plates. The inability of EIT to effectively tackle electrical anisotropy limits its usage in CFRP structures. Moreover, most real structures of complex geometries lack well-defined edges on which electrodes can be placed. Therefore, in this thesis, we confront these limitations by presenting a study into the effect of EIT sensitivity matrix formulation and surface-mounted electrodes on damage detection and localization in CFRPs.

In this work, the conductivity is modeled as being anisotropic, and the sensitivity matrix is formed using three approaches – with respect to i) a scalar multiple of the conductivity tensor, ii) the in-plane conductivity, and iii) the through-thickness conductivity. It was found that through-hole damages can be adeptly identified with a combination of surface-mounted electrodes and a sensitivity matrix formed with respect to either a scalar multiple of the conductivity tensor or the in-plane conductivity. This theory was first validated on a CFRP plate to detect a single through-hole damage. Furthermore, EIT was also used to successfully detect both through-hole and impact damages on a non-planar airfoil shaped structure.

Singular value decomposition (SVD) analysis revealed that the rank of the sensitivity matrix is not affected by the conductivity term with respect to which the sensitivity matrix is formed. The results presented here are an important step towards the transition of EIT-based diagnostics to real-life CFRP structures.

1. INTRODUCTION

Advanced composites have played a major role in reduced fuel consumption in aerospace applications. Moreover, their excellent fatigue and corrosion resistance properties lower their maintenance costs in comparison to most metals. This makes them ideal to be used for large parts such as fuselages and wings of commercial aircrafts. However, a critical disadvantage of composite structures is the inability to easily detect internal or sub-surface damages. Defects in composites can occur at both manufacturing and in-service stages [1]. Manufacturing induced defects usually involve the introduction of voids and resin rich areas. In the operational stage, typical fatigue and environmental conditions can lead to formation of defects. While defects are common in traditional metals as well, in composites they usually lead to internal damages that can go undetected by traditional standards of inspection originally geared toward metallic structures. These damages usually include internal fibre breakage, delaminations, matrix cracking, debonding and many more. Current structural inspection methods commonly involve, for example, ultrasonic, thermography and radiography techniques. Due to the multitude of unique damage modes that exist, none of the current NDT methods are single-handedly capable of identifying all forms of internal damages in composites [2]. Moreover, some of these methods require dismantling and test rigs to accommodate large structures for inspection [3]–[8], leading to service disruptions and further adding to maintenance costs.

In light of these difficulties, as an alternative, structural health monitoring (SHM) can provide a continuous evaluation of the structural integrity of composite structures by tracking the progress of damage in composites in real time in a cost effective manner. Due to the increasing use of composites and the need for continuous monitoring of these materials, the next sub-section briefly summarizes a few prevailing SHM methods for composite materials.

1.1 SHM Techniques

SHM broadly involves implementing a damage identification strategy which does not require the structure or component to be taken out of service. The physics and techniques

involved to localize damage, however, are dependent on the SHM technique utilized. A few different prevailing methods and their detection strategies are discussed below.

Vibration-based SHM of composites is a commonly researched technique. [1], [9]–[13]. Here, the alteration in the vibration response based on weakened mechanical properties such as stiffness and strength due to structural damage is monitored. Properties like frequency, modal shapes and modal damping are analysed to detect damages. However, due to low resolution, this technique is better suited to detect large damages that can significantly change the first few natural frequencies and mode shapes [14].
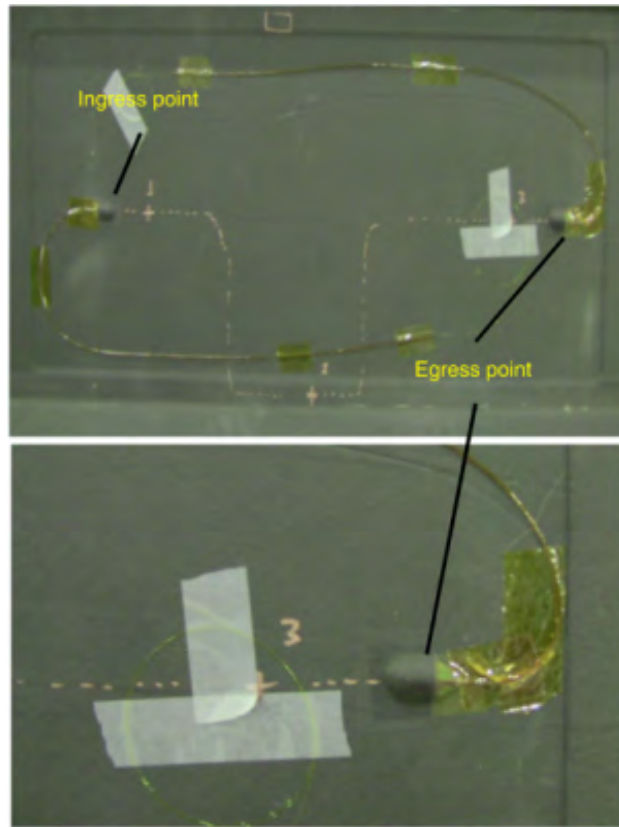
Figure 1.1. Embedded FOBG sensors used to detect impact damages on CFRP fuselage panel as described in [15].

Embedded sensors are also greatly researched to measure strain/temperature changes in composites [16]–[18]. For example, Roman et al. [15] measured changes in strains due to impact damage in CFRP fuselage panels using fibre optic Bragg grating (FOBG) under compressive loads (Figure (1.1)). FOBG sensors can even be built into the composite lam-

inate to allow for internal monitoring. However, positioning of these sensors on and/or in the structure is critical as they can only detect damages at their immediate vicinity.

As an additional example, embedded piezoelectric sensors/actuators can measure variations in the vibrational response of a structure to detect damage [19]–[21]. This can be done either passively (i.e. the piezoelectric just senses vibrations) or actively (i.e. one ore more piezoelectrics inject ultrasonic sound energy and listen for reflections due to damages). Pardo de Vera [22] used this principle to monitor crack growth in GFRPs by making use of PZTs as both actuators and sensors. It was noted that temperature changes diminish the sensing capability of PZTs.
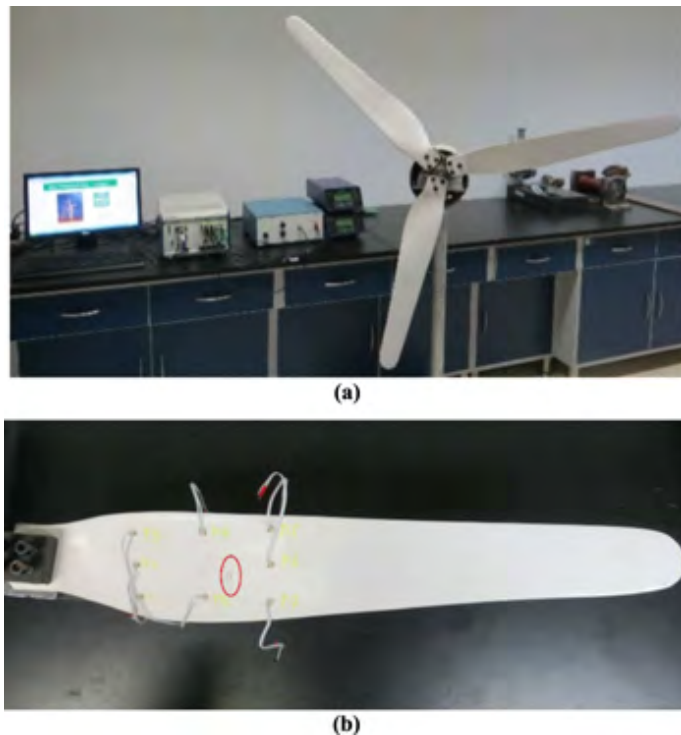
Figure 1.2. (a) Overall experimental setup (b) Experimental wind turbine blade with a crack in the red circle detected through the embedded PZT actuator and sensor network [23].

And as a final representative example, guided wave-based sensing involves propagation of short ultrasonic pulses through composite structures to locate defects [24]–[28]. For example, Liu et al. [23] used a Lamb wave based imaging technique for crack detection in anisotropic turbine blade using a sparse PZT sensor array as shown in Figure (1.2). Guided waves have

shown potential as an SHM modality but still face the disadvantages related to complexities in wave propagation due to multi-modal characteristics, reflections and mode conversions from discontinuities in the structure.

1.2   Self-Sensing Material-Based Monitoring

Self-sensing materials are a promising alternative to traditional SHM because they do not require the addition of external sensing hardware. Rather, they relate changes in an intrinsic material property to the health of the structure [29]–[36]. Nanofiller modified composites have received significant attention in this area of work [37], [38]. Dispersing a small concentration of these nanofillers in an otherwise insulating matrix forms an electrically conductive network. Changes in the conductivity of this network can be an effective approach to monitoring damages in both polymeric and cementitious composites [39]–[43]. For example, as microcracks propagate in the matrix material, the conductive pathways get disrupted at that region, resulting in changes in measured electrical resistance. In addition, well-dispersed nanofillers can impart greater strength to composite structures [38]. Beyond just detecting material rupture, elastic deformations that reorient the nanofiller network likewise manifest as a conductivity change [44]–[46]. This is illustrated in Figure (1.3).

Similarly, with regard to CFRPs, the fractional change in their electric resistance can be measured to detect damages in the structure. In the case of CFRPs, carbon fibres act as the electric conductors in an insulating matrix medium. Any modification in these pathways, either due to elastic strains or damages, can cause changes in the electric resistance which can be captured by electrodes placed on the surface of these structures [48]. In terms of piezoresistive behaviour, it has been found that on applying tensile loads in unidirectional CFRPs, the longitudinal electric resistance decreases reversibly with strain while the transverse resistance increases. The decrease in resistance is attributed to the alignment of fibres in the loading direction which increases electric contact. This further leads to decrease in electric contact in the transverse direction, contributing to increased resistance [49]–[51].

Since carbon fibre/epoxy composites are known to possess low ductility, hybrid composites of carbon and other fibres have also been researched for strengthening and self-sensing

16
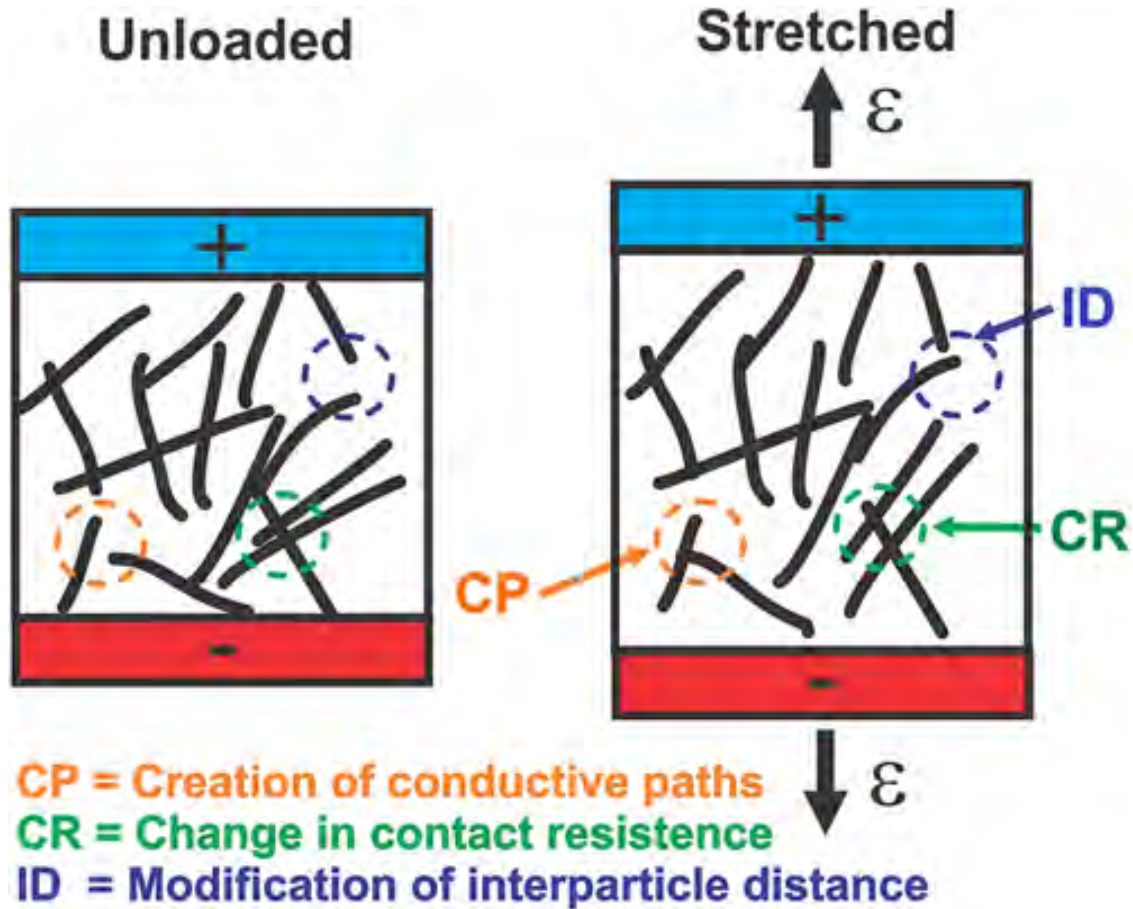
Figure 1.3. A schematic representation of piezoresistive mechanisms in polymer composites of low filler content on applied strain [47].

behaviour [53], [54]. One such example is the use of CF-GF hybrid composite rod to generate alarm signals prior to breakage of the structure as shown in Figure (1.4) [52]. However, many of these materials are incapable of detecting damages at early stages due to insignificant changes in electrical resistance at low strains.

CFRPs have also been successful in monitoring damages that lead to permanent changes in resistance such as fibre breakages and delaminations. For example, Todoroki et al. (Figure (1.5)) monitored delaminations in symmetric carbon fibre composite laminates of different volume fractions. Electric conductance in the thickness direction of the specimens was measured to be one tenth of the conductance in the transverse direction. This led to a gradual flow of electric current in the thickness direction, enabling the detection of delaminations through the resistance change measured between electrodes when current is charged in the
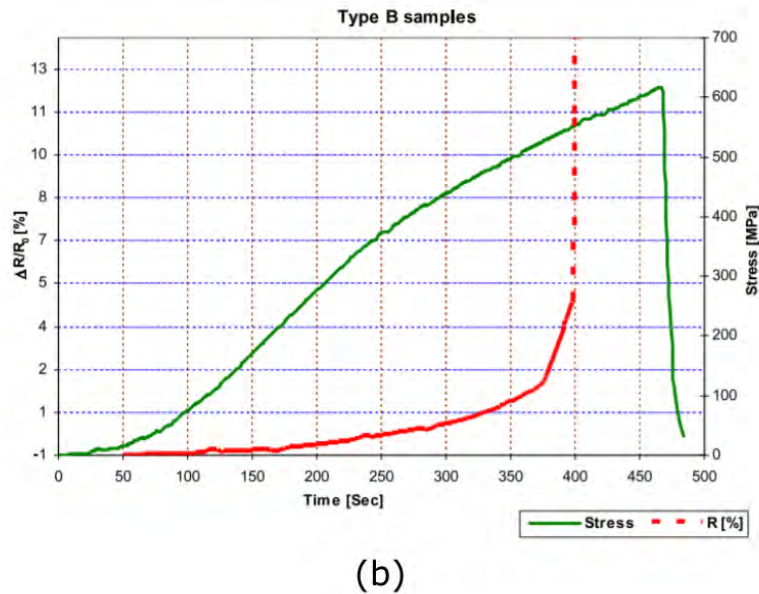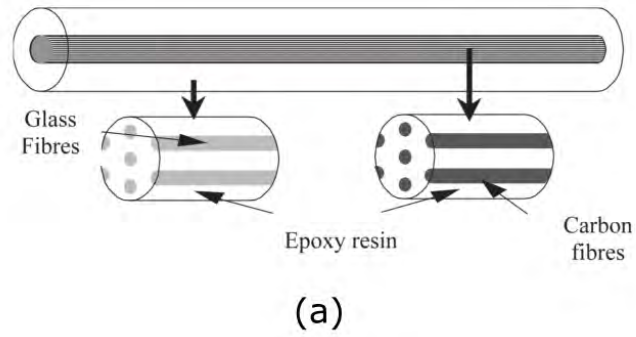
Figure 1.4. (a) Sketch of a CF–GFRP rod containing internal unidirectional carbon fibres externally covered by a glass fibre bundle. Copper electrodes are bonded at the end of carbon rods for testing. (b) Variation in fractional resistance during tensile test of CF-GF hybrid composite [52].

fibre direction. The same damage however, could not be detected when electric currents were charged in the transverse direction.

Additionally, Abry et al. [56] conducted monotonic and cyclic flexural tests on unidirectional CFRP laminates of different volume fractions for comparison. The monotonic tests as seen in Figure 1.6 (2), show a steep rise in electrical resistance due to ply failure in the composite with the lowest volume fraction. For larger volume fractions, we see a progressive change in resistance. This is due to a significant part of the conduction occurring at the

18
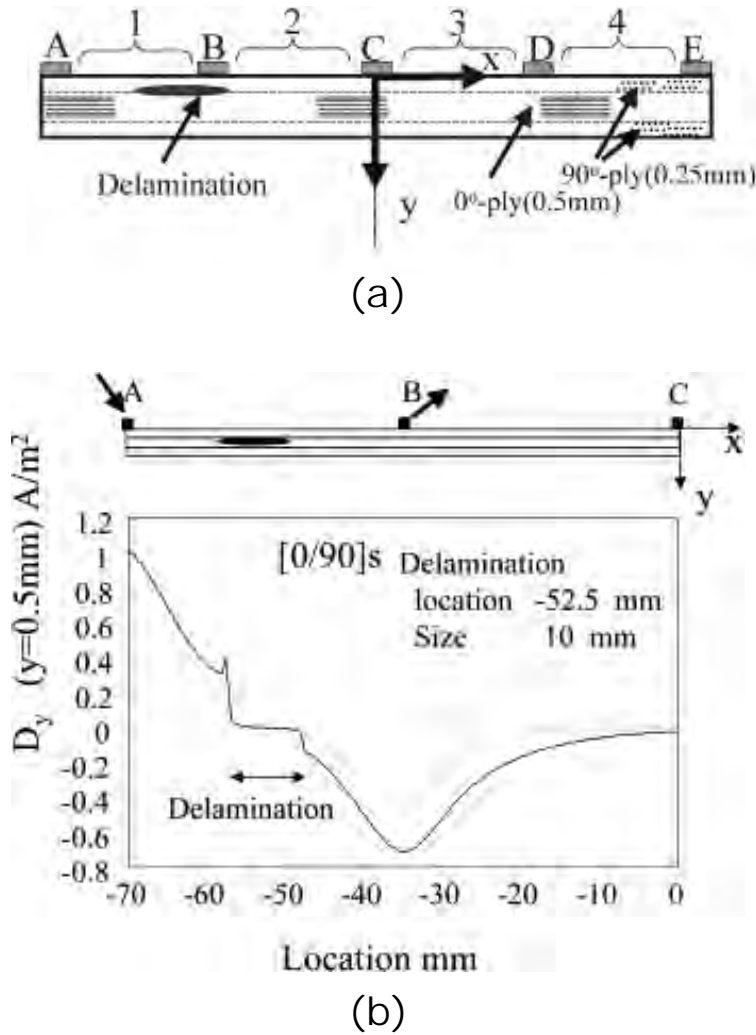
Figure 1.5. (a) Specimen configuration of $[0/90]_s$ laminate with electrodes A-E placed on the surface. (b) Electric current density of the thickness direction (Dy) at the cross section of y=0.5 mm between electrodes A and C [55].

inner layers of the composite, making the contribution of first plies to overall conduction less pronounced. It was concluded that sensitivity of damage detection is dependent on both electrode placement and fibre volume fraction.

And as a final representative example, Swait et al. [57] incorporated printed circuit boards into panels to successfully monitor the resistance changes due to barely visible impact damages (BVID) in CFRPs. In this study, electric contact was provided by interleaving the PCB with carbon fibre plies. The resistance between the opposite pairs of contacts was measured before and after impact loads to detect BVIDs. It was found that wider contacts

(1)

(2)
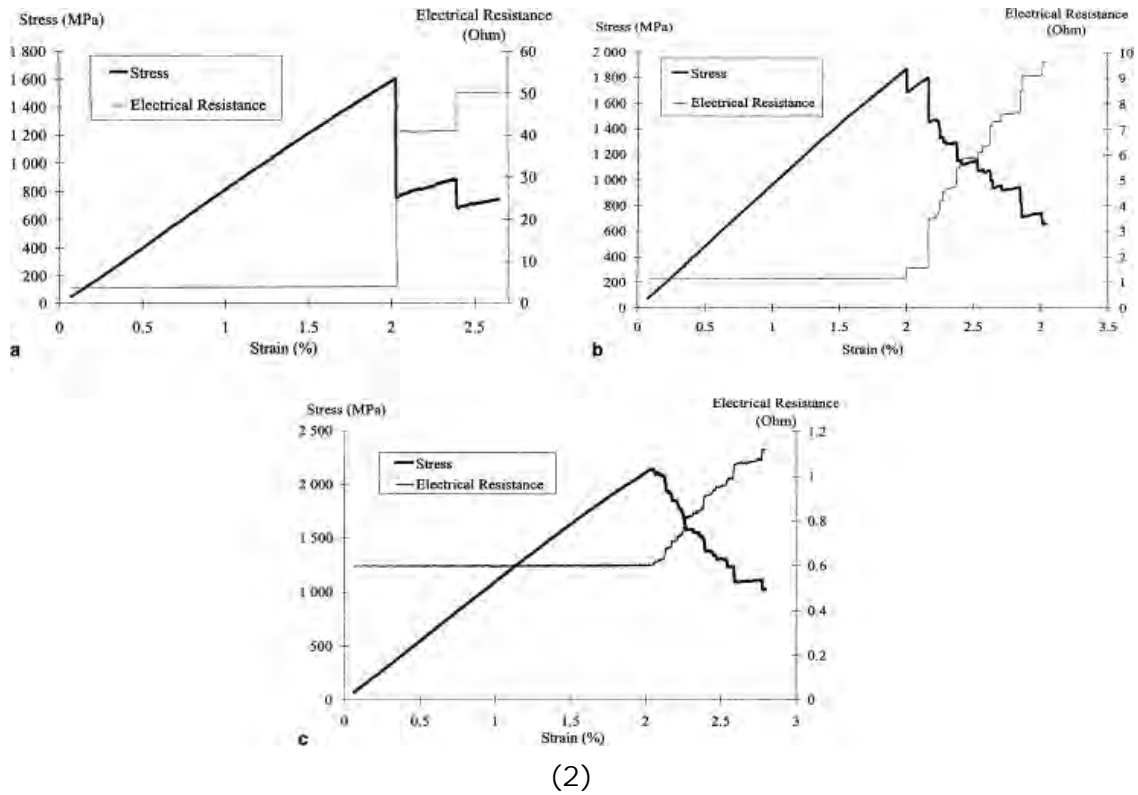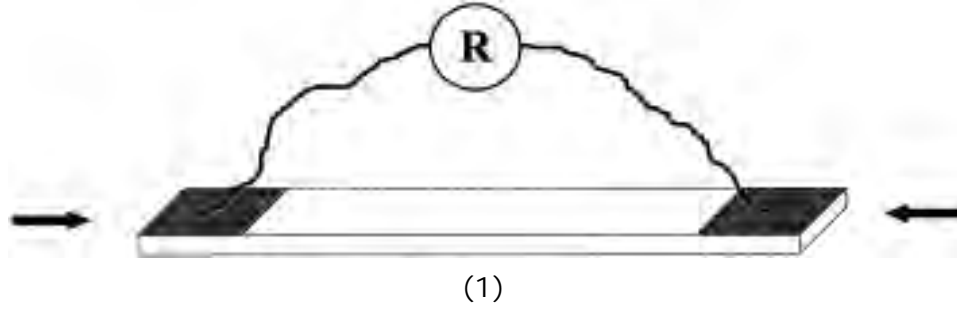
Figure 1.6. (1) Schematic representation of electrodes placed at the ends of specimen for mechanical testing. (2) Changes in stress and electrical resistance as a function of the applied strain during a flexural monotonic loading. (a) $V_f = 0.43$, (b) $V_f = 0.49$ and (c) $V_f = 0.58$ [56].

reduced sensitivity to damages but did provide greater consistency in baseline resistances. Additionally, damage was successfully detected in panels up to 1 m in length.
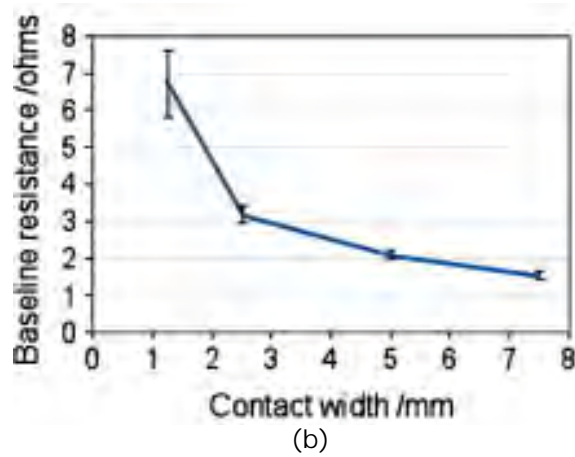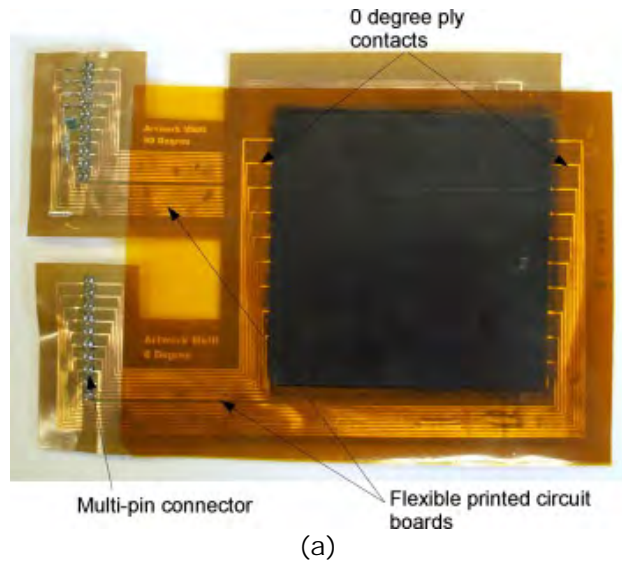
Figure 1.7. (a) CFRP panel containing flexible printed circuit boards as interleaves for connection with the two plies of the laminate. (b) Lowered standard deviation of measured baseline resistance for wider contact widths [57].

1.3 EIT-Based Damage Detection in CFRPs

While resistance change methods as summarized in the preceding sections work well to detect damages, they provide poor spatial localization. Electrical impedance tomography (EIT)-based SHM allows for spatially mapping these damages for better visualization. EIT was first known to be developed for biomedical applications [58], [59]. Over the years, it has been explored for NDE and SHM [60], where it is able to resolve damage-induced conductivity changes from domain boundary voltage. For example, EIT has been used to

image conductivity distributions in both cement-based composites as well as polymer-based composites using self sensing skins [61]–[63]. Any deformation/damage on material surface to which these skins are adhered to leads to a detectable localized change in conductivity in these skins.

To date in NDE and SHM, EIT has also been mostly employed in materials of low anisotropy such as nanofiller-modified polymers to detect various modes of damage. These materials are imparted self-sensing capabilities by dispersing nanofillers into the matrix material to form conductive pathways [64]–[66]. For example, Tallman et al. [67] were able to clearly image both through-hole damages as small as 3.18 mm in diameter as well as impact damages in glass fibre/epoxy plates with CB filler (Figure (1.8) and (1.9)).
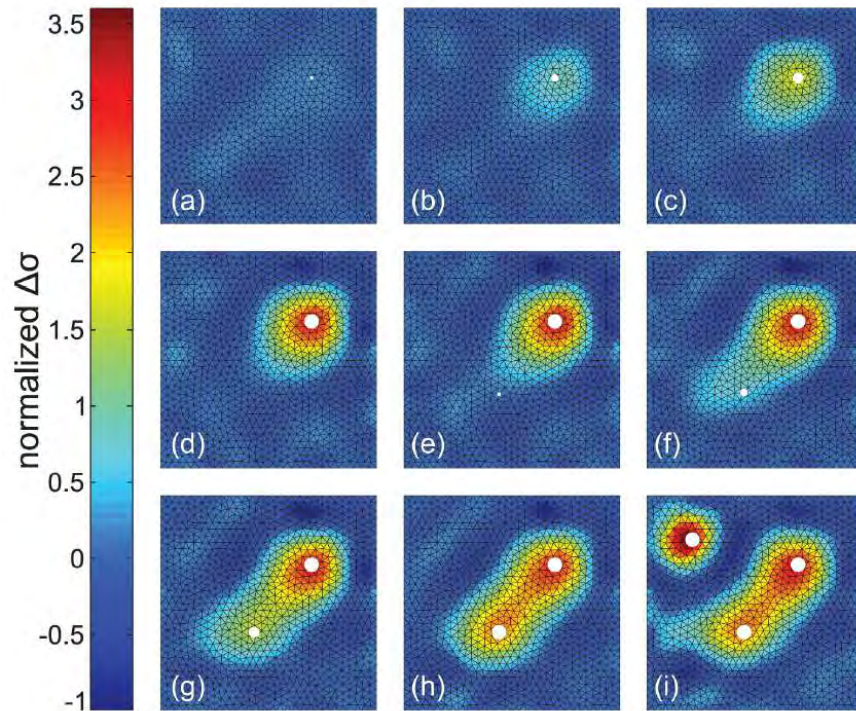
Figure 1.8. Through-hole size and location are indicated by white circles for damage detection in a carbon black-modified glass fiber/epoxy laminate. Diameters of each through hole are as follows: (a) 1.59 mm, (b) 3.18 mm, (c) 4.76 mm, (d) 6.35 mm, (e) 6.35 mm and 1.59 mm, (f) 6.35 mm and 3.18 mm, (g) 6.35 mm and 4.76 mm, (h) 6.35 mm and 6.35 mm, and (i) 6.35 mm, 6.35 mm and 6.35 mm [67].
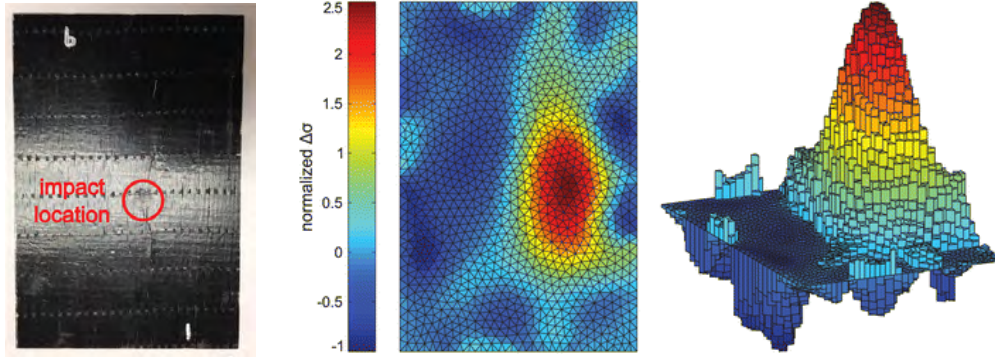
Figure 1.9. EIT image of post-impact damage detection in a carbon black-modified glass fiber/epoxy laminate [67].

With regard to non-planar structures, EIT has also been successful in reconstructing through-hole and BVID in non-planar CB-modified GF/epoxy tubes of different aspect ratios as shown in Figure (1.10). It is seen that for a tube of aspect ratio 2:1, holes close to the center of the specimen went undetected whereas those close to the electrodes were easily detected. Following this, it was found that for a lower length of the tube (with an aspect ratio of 1:1), damages at the center could be localized.

Work in EIT applied to CFRPs is not yet as prevalent as for nanocomposites due to the added complexity of highly anisotropic conductivity in these materials. As early as 2001, Schueler et al. [69] investigated the use of EIT for damage detection in unidirectional single ply CFRP laminates by placing 16 razor blade electrodes at the edges of the specimens. For an anisotropy ratio of 2000, they endeavoured to detect three square holes by mapping the voltage differences between those measured before and after inducing damage. They found good agreement between numerical predictions and experimental results to conclude that the shift in potential peaks correspond to the position of the holes as illustrated in Figure (1.11). However, they did not use the traditional EIT formulation.

Work was also done to detect and map tensile damage in plain-weave CFRPs by utilizing a spray-on nanocomposite sensor [70]. This sensor consisted of a film containing electrically percolated distribution of carbon nanotubes in a polyvinylidene flouride latex. Prior to spraying this film onto the CFRP, the surface of the sample was coated with epoxy and cured to ensure the conductive carbon fibre does not interfere. In this case, the film itself
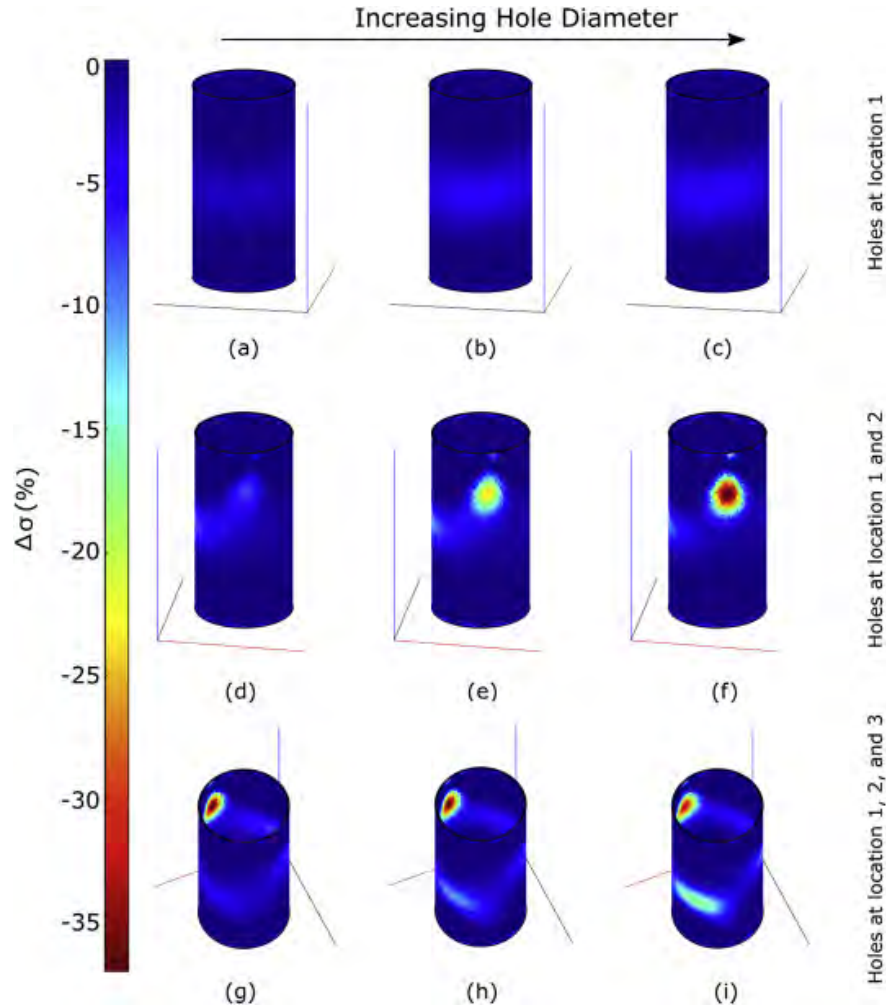
Figure 1.10. EIT reconstructions of (a) 4.76 mm hole at location 1, (b) 7.94 mm hole at location 1, (c) 9.53 mm hole at location 1, (d) 4.76 mm hole at location 2, (e) 7.94 mm hole at location 2, (f) 9.53 mm hole at location 2, (g) 4.76 mm hole at location 3, (h) 7.94 mm hole at location 3, and (i) 9.54 mm hole at location 3. A colored triad is included to help orient the reader to rotations of the tube [68].

acts as the sensor rather than the actual CFRP. Nevertheless, electrical conductivity maps for these samples were obtained for varying levels of strain and damage as shown in Figure (1.12).

Baltopoulous et al. [71] reconstructed damages of both through-hole and indentation type in CFRPs using edge-placed electrodes. In this study, three layered CFRP made of woven twill fabric was used. On measuring the in-plane conductivity in 0° , 30°, 45°, 60°
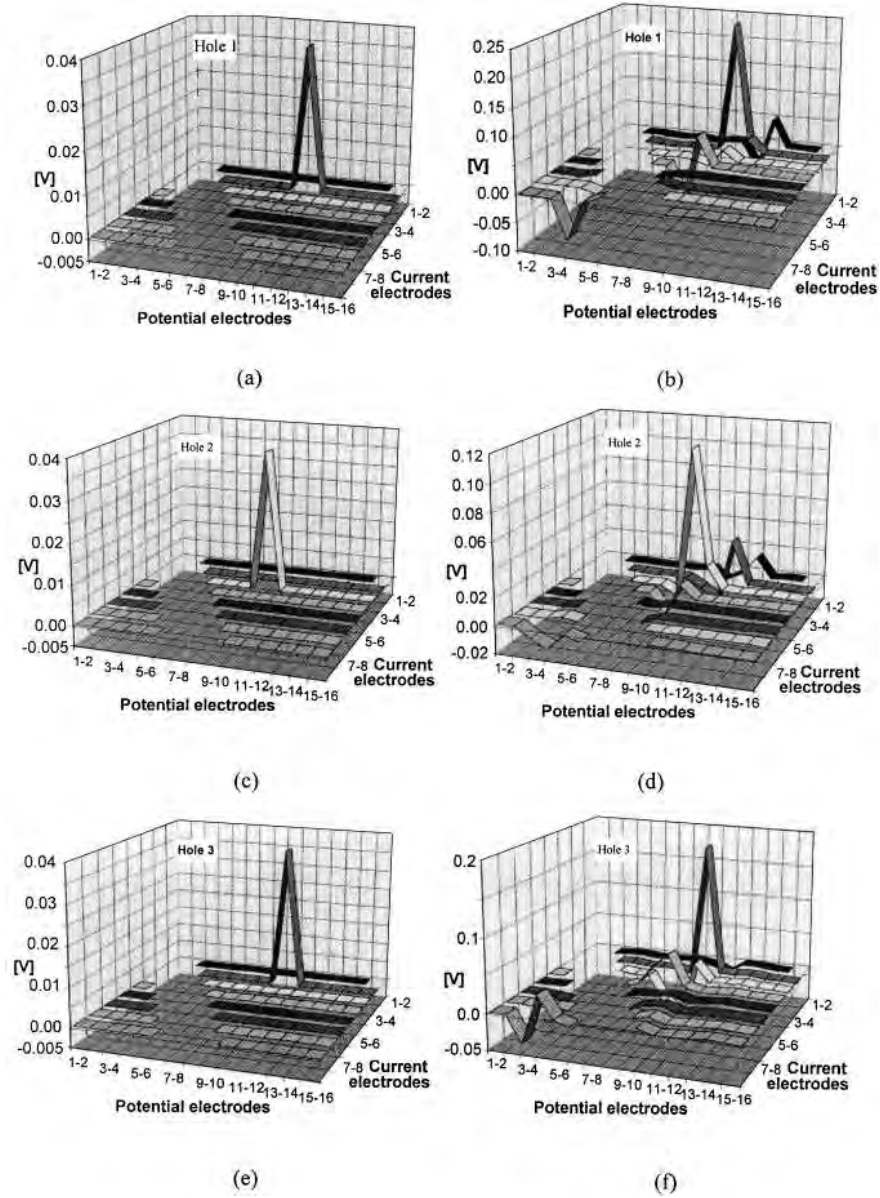
Figure 1.11. A comparison of numerical (a,c,e) and experimental results (b,d,e) where the peaks correspond to position of the 3 holes in the horizontal space [69].

and 90° directions, it was noted that the plates exhibited electrically isotropic conductive properties. Thus, it was modelled as a homogeneous and isotropic material. They utilized the L-curve to find the optimal hyper-parameter value, λ, for the best rendering of the conductivity distribution of the square laminate with a 3 mm hole (Figure (1.13)). It was concluded that holes of 0.1% of the total monitored area can be detected.
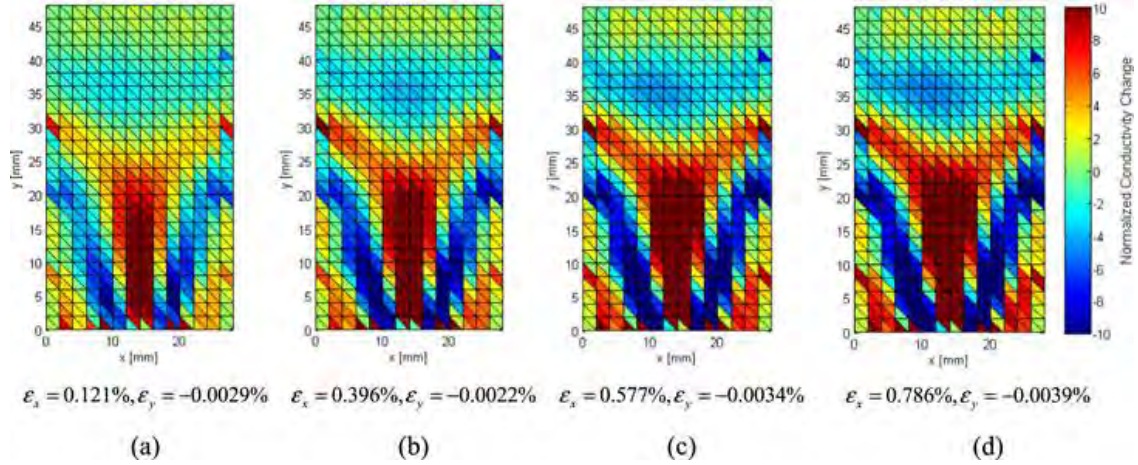
Figure 1.12. [70] Electrical conductivity maps for CFRPs on varying levels of strain and damage due to tensile loading.
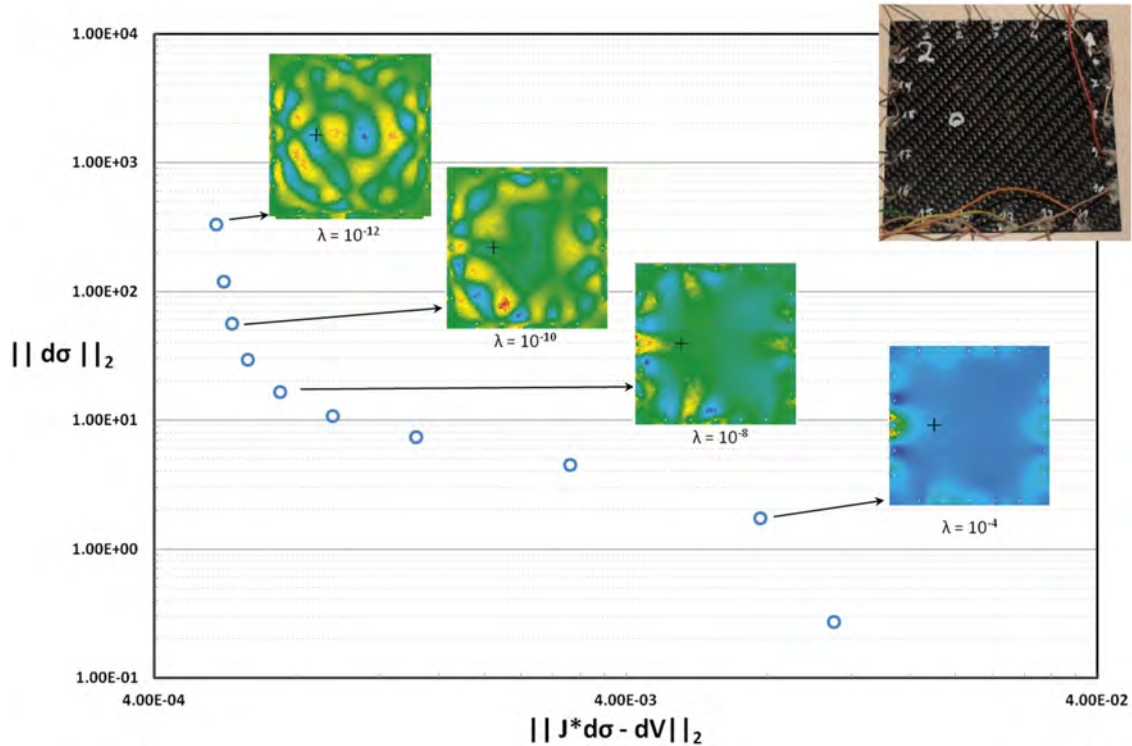
Figure 1.13. Conductivity maps and L-curve for through-hole damage case: calculated conductivity change maps for various λ-values (the cross indicates the point of damage) in CFRP laminate [71].

Nonn et al. [72] investigated different current injection patterns and their effects on the quality of damage reconstructions (Figure (1.14)). In this case, aluminum rivets were

26

used as edge-placed electrodes on unidirectional CFRP laminates. Since anisotropy of the material was not considered in the inverse model, there exists inherent error in the reconstructions. From the results obtained, it was concluded that opposite and diagonal injection patterns yield minimum position errors. Furthermore, they discovered that picking a high hyper-parameter value in case of a diagonal current injection pattern helps smooth out the conductivity change to be concentrated around the damaged location. It was concluded that the anisotropy presented in unidirectional CFRPs needs to be incorporated in the reconstruction algorithm in order to obtain distinct localizations.
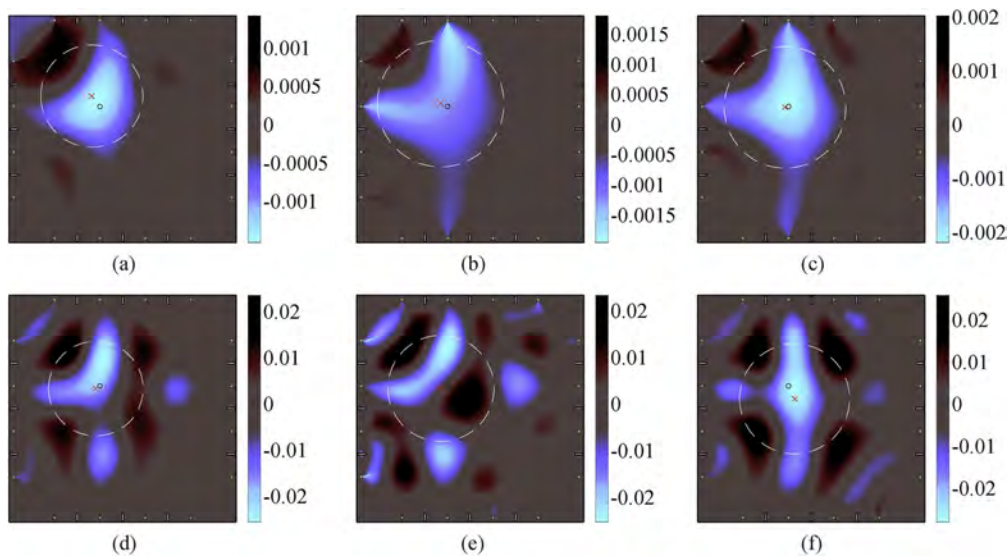
Figure 1.14. Reconstructed conductivity change in CFRP laminate for three different current injection patterns and different hyperparameters λ: (a) Adjacent, (b) Opposite, (c) Diagonal, (d) Adjacent, (e) Opposite, (f) Diagonal. The black circle indicates the defect position (5 mm hole), the red cross is the center of gravity of the minimum one-forth amplitude set (white circle) [72].

Cagáň et al. [73] incorporated a Gaussian anisotropic smoothing filter as a priori information to adeptly detect cuts on CFRP plates of quasi-iostropic, orthotropic and asymmetric layups as shown in Figure (1.15). In this case, 24 edge-placed electrodes were utilized with an opposite current injection pattern. It was found that cross-correlation coefficients of the anisotropic filter (a comparison parameter) increased by approximately twice in comparison to those obtained for isotropic filter. Additionally, the solution error parameter is improved

by the smoothing filter by 5-10%. These parameters confirm the effectiveness of the filter in damage detection.

Furthermore, Cagáň et al. [74] also used EIT to detect BVIDs in carbon fibre plates of quasi-isotropic, orthotropic and asymmetric layup as shown in Figure (1.16). From the reconstructed images of the conductivity changes, the amplitudes and the position errors for different image priors were evaluated. Amplitudes were related to the area of delamination obtained by C-scan and assessed statistically by probability of detection curves. The presented amplitude sensitivity and position error allows EIT to be considered as a SHM tool for early detection of BVIDs.

Table 7. Examples of the image reconstructions obtained with the isotropic (ISO) and anisotropic (ANISO) Gaussian smoothing filters (green elements indicate the HA set, whereas the red line indicates the nominal position of the crack).
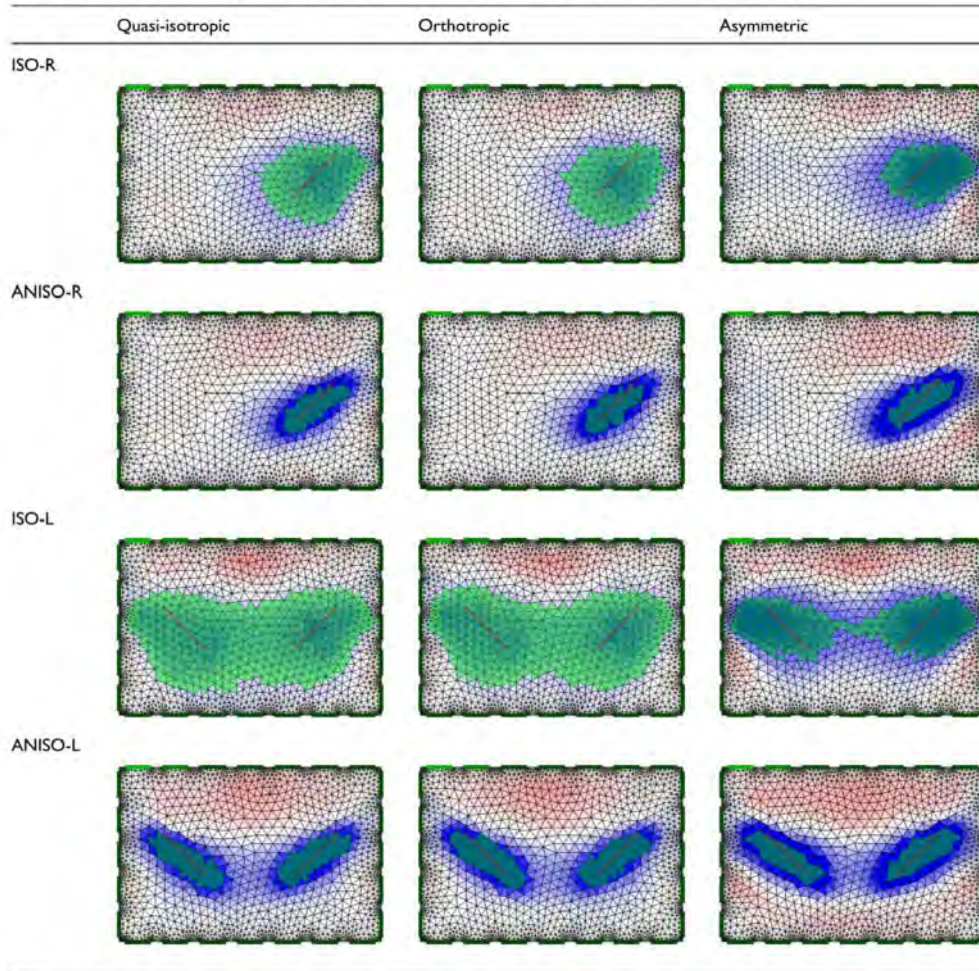
HA: half-amplitude.

Figure 1.15. Examples of the image reconstructions obtained with the isotropic (ISO) and anisotropic (ANISO) Gaussian smoothing filters (green elements indicate the HA set, whereas the red line indicates the nominal position of the crack) [73].
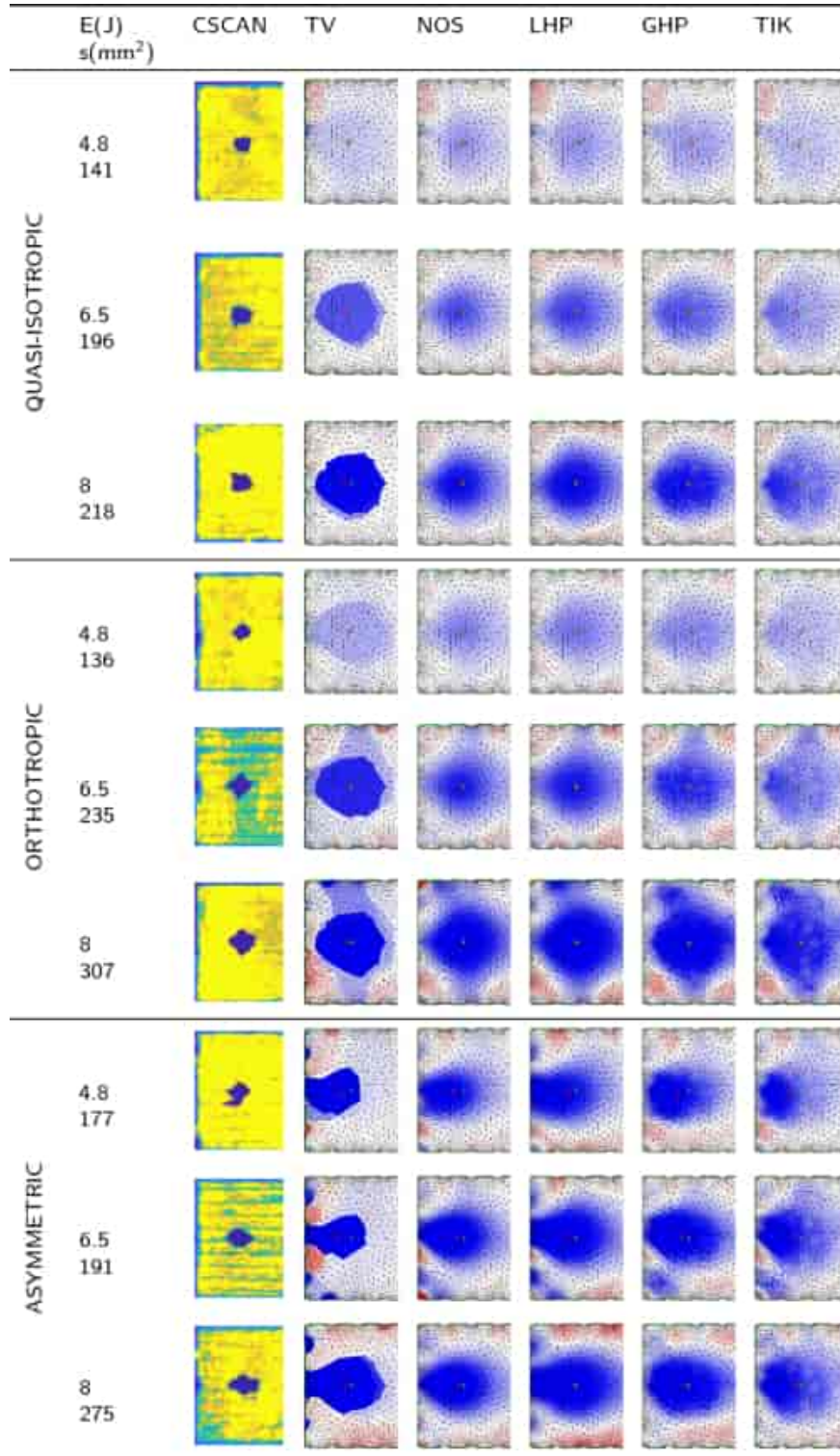
Figure 1.16. Overview of some typical image reconstructions across individual stacking sequences (quasi-isotropic, orthotropic, asymmetric) and image priors (TV total variation, NOS Newton's One-Step Error Reconstructor, LHP laplace 2nd order high pass filter, GHP Gaussian high pass filter, TIK - Tihkhonov) related to C-scan images and areas of delamination [74].

2. PROBLEM STATEMENT AND RESEARCH GOAL

In light of the preceding discussion, we can see that while a great deal of work exists on the topic of EIT for SHM, the body of literature overwhelmingly favors nanocomposites. Further research is still needed to adeptly transition EIT to CFRPs. Even more work is needed for non-planar, structurally realistic geometries (i.e. the majority of studies to date consider only simple flat plates with edge-mounted electrodes). From this, the following Problem Statement and Research Goal are formulated.

2.1 Problem Statement

Due to their high strength-to-weight ratio, corrosion resistance and scalability, CFRPs are becoming increasingly common in weight-conscious applications like aerospace. However, effective damage detection is challenging in CFRPs. Electrically based methods like EIT are promising because they leverage inherent self-sensing capabilities in CFRPs, thereby eliminating the need for ancillary sensing equipment. Unfortunately, EIT has not been nearly as widely explored in CFRPs as nanocomposites due to challenges associated with electrical anisotropy. Furthermore, prevailing EIT studies make use of unrealistic edge-mounted electrodes which would be difficult to replicate in practice. These challenges need to be overcome if EIT is to see widespread embrace for CFRP SHM and diagnostics.

2.2 Research Goal

The goal of this research is to explore modifications to the existing EIT mathematical framework in order to better accommodate the anisotropic conductive properties of CFRPs. Specifically, this work explores the concept of directional sensitivity matrices in EIT – sensitivity matrix formed with respect to specific conductivity components of an anisotropic conductivity tensor. Additionally, this work will explore surface-based electrode placement schemes for non-planar geometries. The combination of the above two conditions shall further the potential of EIT as a SHM modality for CFRPs.

2.3 Thesis Organization

Based on the problem statement and research goal, the remaining of this thesis is organized as follows. First, a brief introduction to the mathematical framework of EIT will be presented along with the sensitivity matrix formulation unique to this work. Second, the experimental procedure including the manufacturing and experimental setup of planar and non-planar CFRP structures will be discussed. Third, the results from through-hole and impact damage testing will be presented in detail. And lastly, this thesis concludes with a summary, conclusions, and a discussion on future work.

3. ELECTRICAL IMPEDANCE TOMOGRAPHY

3.1 Introduction

EIT is an imaging modality that maps internal conductivity distributions of domains based on current-voltage relations obtained at the boundaries. In composites, the development of damage over time leads to a loss of conductivity. Therefore, EIT has potential to monitor damage in conductive composite material systems. EIT is composed of two parts – a forward problem and an inverse problem. Experimentally, a domain is subject to a series of current injections between a chosen sequence of electrode pairs while voltage is collected between electrode pairs not involved in the current injection. In the difference imaging approach used here, we shall take voltage measurements at both pre-damage and post-damage states of the domain. Since voltage measurements are sensitive to conductivity changes, the difference in these measurements will be used to localize the damage. The forward problem as described below involves computationally replicating the same experimental process to obtain identical voltage vectors using the finite element method. The inverse problem then involves minimizing the difference between the voltage measurements collected from the experimental procedure to obtain the conductivity distribution.

Below, the general formulations of the forward and the inverse problem are discussed. The modifications in terms of sensitivity matrix formulations to address the anisotropy of CFRPs is covered as well. While open-source EIT routines do exist (e.g. EIDORS [75], [76]), all EIT code used in this research was developed in-house using Matlab.

3.2 Forward Problem

As mentioned above, EIT consists of a forward problem and an inverse problem. The forward problem is the process of simulating current flow in the domain. For steady-state diffusion in the absence of internal sources, the relation between current and domain potential is defined by the Laplace equation as shown in equation (3.1). Here, σ_{ij} represents the

anisotropic conductivity and u represents the domain potential. Note that repeated indices imply summation over the dimension of the domain except where noted otherwise.

$$\frac{\partial}{\partial x_i}\sigma_{ij}\frac{\partial u}{\partial x_j} = 0 \tag{3.1}$$

The complete electrode model boundary conditions are applied to simulate contact between the perfectly conducting electrodes and the domain as shown in equation (3.2). Equation (3.3) enforces the principle of conservation of charge which requires the net current through the electrodes to sum to zero. Note that a summation is not implied over repeated ls in equation (3.2).

$$\sigma_{ij}\frac{\partial u}{\partial x_i}n_j = \frac{1}{z_l}(V_l - u) \tag{3.2}$$

$$\sum_{l=1}^{L}\int_{E_l}\sigma_{ij}\frac{\partial u}{\partial x_i}n_j \, \mathrm{d}S_l = 0 \tag{3.3}$$

Here, n_j denotes an outward pointing normal vector, z_l the contact impedance of the lth electrode, E_l the area of the lth electrode and V_l the voltage of the lth electrode. The finite element method is used to solve the above three equations as shown in equation (3.4). $\boldsymbol{U}$ represents the vector of domain potentials, $\boldsymbol{V}$ the vector of electrode voltages and $\boldsymbol{I}$ the vector of injected currents. Summation over l is not implied in equations (3.7) and (3.8).

$$\begin{bmatrix} \boldsymbol{A}_M + \boldsymbol{A}_Z & \boldsymbol{A}_W \\ \boldsymbol{A}_W^T & \boldsymbol{A}_D \end{bmatrix}\begin{bmatrix} \boldsymbol{U} \\ \boldsymbol{V} \end{bmatrix} = \begin{bmatrix} \boldsymbol{0} \\ \boldsymbol{I} \end{bmatrix} \tag{3.4}$$

$$A_{M\ ij}^{e} = \int_{\Omega_e}\frac{\partial w_i}{\partial x_k}\sigma_{kl}\frac{\partial w_j}{\partial x_l} \, \mathrm{d}\Omega_e \tag{3.5}$$

$$A_{Z\ ij} = \sum_{l=1}^{L}\int_{E_l}\frac{1}{z_l}w_i w_j \, \mathrm{d}S_l \tag{3.6}$$

34

$$A_{W\,li} = -\int_{E_l} \frac{1}{z_l} w_i \; \mathrm{d}S_l \tag{3.7}$$

$$A_D = \mathrm{diag}\left(\frac{E_l}{z_l}\right) \tag{3.8}$$

The matrices $\boldsymbol{A}_M$, $\boldsymbol{A}_Z$, $\boldsymbol{A}_W$ and $\boldsymbol{A}_D$ are formed as shown in equations (3.5), (3.6), (3.7) and (3.8), respectively. $A^e_{M\,ij}$ represents the local diffusion stiffness, where the ijth entry refers to the ith row and jth column corresponding to the eth element. The $\boldsymbol{A}_Z$, $\boldsymbol{A}_W$ and $\boldsymbol{A}_D$ matrices account for the additional degrees of freedom introduced by the electrode voltages and the contact impedance between the electrodes and the domain. w_i refers to the ith finite element interpolation function.
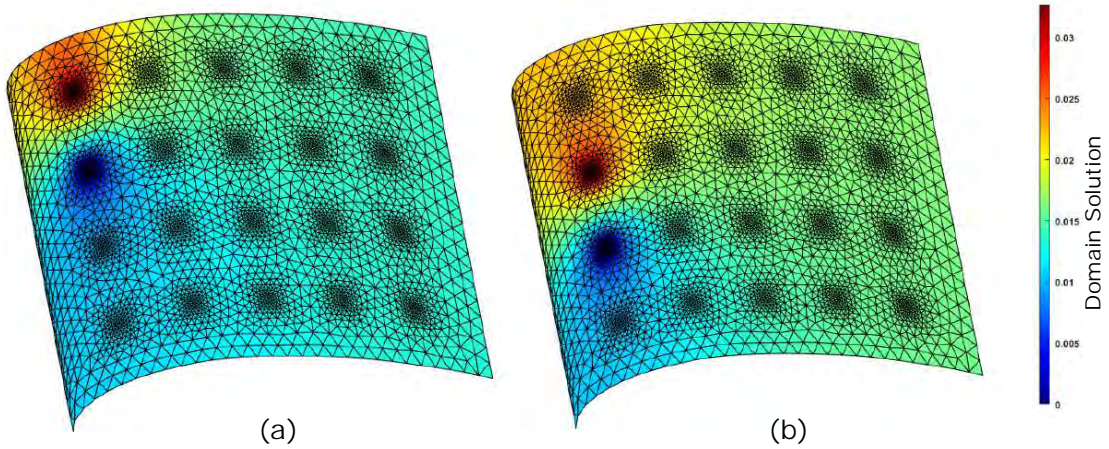
Figure 3.1. Representative solutions of the forward problem on an airfoil geometry using linear tetrahedral elements where (a) current is injected and grounded at the first pair of electrodes (b) current is injected and grounded at the second pair of electrodes.

The above equations and relations were obtained from [64]. Note that we use a 3D mesh with linear tetrahedral elements for non-planar shapes. There does exist very recent work on 2D models for non-planar geometries [77]; however, this is limited to detecting surface damages using sensing skins which have nearly zero thickness. This may be inadequate for laminates of decidedly finite thickness.

3.3 Inverse Problem

While numerous algorithms exist in literature for image recovery via EIT (e.g. utilizing different error and regularization norms [78], iterative non-linear difference imaging methods [79] and direct d-bar methods [80]), in this study we shall focus on the one-step minimization in the least squares sense to obtain the conductivity change in the domain. This method is selected because it is well known to be robust against experimental noise while providing satisfactory imaging capabilities.

3.3.1 Formulation of the General One-Step Minimization

In the inverse problem, we intend to use difference imaging to minimise an error vector in the least squares sense as shown in equation (3.9). We adopt the difference imaging method to subtract out the errors arising from discrepancies between the experimental setup and the finite element model, such as misplaced electrodes or domain shape.

$$\Delta\boldsymbol{\sigma}_{ij}^* = \operatorname*{arg\,min}_{\Delta\sigma_{ij}} \|\boldsymbol{V}_m - \boldsymbol{W}\left(\Delta\boldsymbol{\sigma}_{ij}\right)\|_2^2 \tag{3.9}$$

Here, $\Delta\boldsymbol{\sigma}_{ij}$ is a slight abuse of index notation and can be thought of as a vector of conductivity tensors where each element of the vector corresponds to an element in the forward problem mesh. $\Delta\boldsymbol{\sigma}_{ij}^*$ is a conductivity distribution satisfying the minimization. $\boldsymbol{V}_m$ represents the difference between experimental voltages measured at the domain boundary before and after damage. Let these be denoted as $\boldsymbol{V}_{t_1}$ and $\boldsymbol{V}_{t_2}$ as shown in equation (3.10). Similarly let $\boldsymbol{W}$ represent the computationally predicted difference vector as shown in equation (3.11). Here, $\boldsymbol{F}(\cdot)$ is a vector of electrode voltages predicted via the forward problem described previously. For the case of isotropic conductivity, we would approximate this computationally predicted difference vector using a Taylor series expansion centered about an initial conductivity estimate. A similar expansion could be done in the anisotropic case, but it presents a problem. That is, the isotropic EIT inverse problem is severely ill-posed. This ill-posedness is exacerbated for anisotropic conductivity because the number of unknowns has increased from one per element to six per element in 3D since the conductivity tensor

is symmetric (two unknowns per element in 2D). Methods of overcoming this challenge are described in the next sections.

$$\boldsymbol{V}_m = \boldsymbol{V}_{t_2} - \boldsymbol{V}_{t_1} \tag{3.10}$$

$$\boldsymbol{W} = \boldsymbol{F}\left(\boldsymbol{\sigma}_{ij}^2\right) - \boldsymbol{F}\left(\boldsymbol{\sigma}_{ij}^1\right) \tag{3.11}$$

3.3.2 Sensitivity Matrix Formulation

Due to the ill-posed nature of the EIT problem, a unique solution to anisotropic EIT does not exist (i.e. cannot find all independent components of an anisotropic conductivity tensor). Therefore, a common approach is to instead seek some scalar multiple of the conductivity tensor. This is most often done by extracting a multiplicative factor from the conductivity tensor that preserves its eigen vectors [81], [82]. In this approach, the conductivity tensor is rewritten as $\sigma_{ij} = \kappa \bar{\sigma}_{ij}$ where the value of κ is chosen such that $\det|\bar{\sigma}_{ij}| = 1$. Hence, instead of finding the independent components of the conductivity tensor, we seek a scalar field solution. The sensitivity matrix (i.e. the derivative term that arises from the linearization process) is then formed as $\boldsymbol{J}^{\kappa} = \partial(\boldsymbol{\kappa}\bar{\boldsymbol{\sigma}}_{ij})/\partial\boldsymbol{\kappa}$ and the solution to the inverse problem is formed as shown below in equation (3.12). Note that $\boldsymbol{\kappa}$ and $\bar{\boldsymbol{\sigma}}_{ij}$ are again boldfaced to indicate that they are defined element-wise in a finite element mesh. Here, constraints are enforced based on predicted range of $\boldsymbol{\kappa}$. The lower limit accounts for the maximum possible loss in conductivity at region of damage (i.e. conductivity cannot decrease by more than 100%, $\boldsymbol{\Delta\kappa} = -\boldsymbol{\kappa}$) while the upper limit is set at 1% greater than the baseline or undamaged conductivity in order to provide some tolerance for noise in the experimental data.

$$\boldsymbol{\Delta\kappa}^* = \min_{-\kappa \leq \Delta\kappa \leq 0.01\kappa} \left\| \begin{bmatrix} \boldsymbol{J}^{\kappa} \\ \alpha\boldsymbol{L} \end{bmatrix} \boldsymbol{\Delta\kappa} - \begin{bmatrix} \boldsymbol{V}_m \\ \boldsymbol{0} \end{bmatrix} \right\|_2^2 \tag{3.12}$$

Due to the ill-posed nature of the inverse problem, a regularization term $\boldsymbol{L}$ is needed to recover physically meaningful conductivity distributions. The discrete Laplace operator is

employed for regularization in this work, which is formed as shown in equation (3.13) (note that the indices here do not imply index notation).

$$\boldsymbol{L} = L_{ij} = \begin{cases} \mathrm{degree}(\Omega_e) & \text{if} \quad i = j \\ -1 & \text{if} \quad i \neq j \quad \text{and} \quad \Omega_e \quad \text{is adjacent to} \quad \Omega_i \\ 0 & \text{otherwise} \end{cases} \qquad (3.13)$$

$\boldsymbol{L}$ is a square matrix with rows and columns equal to the number of elements in the EIT reconstruction finite element mesh (i.e. the mesh on which the conductivity distribution is reproduced). Diagonal elements of the matrix are equal to the number of elements that share a face with the ith element. Else if the ith and the jth elements share a face in three dimensions, $L_{ij} = L_{ji} = -1$. All other values in the matrix go to zero. The discrete Laplace operator is used for regularization because it promotes spatially smooth solutions and penalizes highly oscillatory terms which may arise due to noise.

An explicit equation for the sensitivity matrix used in this approach, $\boldsymbol{J}^\kappa$, is given in equation (3.14) [83]. This relates the electrode voltage perturbations to conductivity perturbations.

$$J^\kappa_{MN\,e} = -\int_{\Omega_e} \frac{\partial u^M}{\partial x_i} \bar{\sigma}^e_{ij} \frac{\partial \bar{u}^N}{\partial x_i} \, \mathrm{d}\Omega_e \qquad (3.14)$$

Here, MN is a single index of $\boldsymbol{J}^\kappa$ and refers to the integral of contraction of the gradient of the voltage on the eth element due to the current supplied by the Mth electrode injection pair and the gradient of the voltage on the Nth adjoint field. In this case, the adjoint field is the solution of domain obtained by unit current injection being supplied to the Nth electrode measurement pair. The integral is evaluated over eth element. The Jacobian can be thought of as the sensitivity measure of the Nth electrode measurement pair due to a slight conductivity change of the eth finite element when the current is injected in the Mth electrode pair. A super-script κ is added to denote this particular sensitivity matrix formulation since more will be defined later.

Although this scalar coefficient approach is often used for imaging of anisotropic media, it fails to incorporate knowledge of the reduction in conductivity with respect to a particular

direction of anisotropy. This information could potentially help distinguish between different modes of damage that exist in composite failure. In other words, the solution tends to be skewed in the principal directions of σ_{ij}, and there is no physical expectation that damage preserve the eigen values of the conductivity tensor. As an alternative, we are interested in the development of sensitivity matrices formed with respect to in-plane and out-of-plane conductivities. This allows for some physical insight to be encoded into the sensitivity matrix. For example, it is expected that damages that impede in-plane current flow between electrodes will be more easily found via an in-plane sensitivity matrix. These sensitivity matrices take the form of $\boldsymbol{J}_{\parallel} = \partial \boldsymbol{F}(\boldsymbol{\sigma}_{ij})/\partial \boldsymbol{\sigma}_{\parallel}$ and $\boldsymbol{J}_{\perp} = \partial \boldsymbol{F}(\boldsymbol{\sigma}_{ij})/\partial \boldsymbol{\sigma}_{\perp}$ where $\boldsymbol{\sigma}_{\parallel}$ is the in-plane conductivity and $\boldsymbol{\sigma}_{\perp}$ is the through-thickness conductivity of the laminate. This is shown in equation (3.15) where the one and two-directions are assumed to be in-plane and the three-direction is assumed to be out-of-plane. Here, σ_{ij} represents the initial conductivity tensor estimate. Solutions to the inverse problem under these conditions are shown below in equations (3.16) and (3.17) with applied constraints. Realistically, the range of conductivity change lies between a 100% loss in directional conductivity value to no change at all. However, to allow for noise in the voltage measurements, we again provide a 1% tolerance on the upper bound to account for a positive change.

$$\boldsymbol{\sigma}_{ij} = \begin{bmatrix} \boldsymbol{\sigma}_{\parallel} & 0 & 0 \\ 0 & \boldsymbol{\sigma}_{\parallel} & 0 \\ 0 & 0 & \boldsymbol{\sigma}_{\perp} \end{bmatrix} \tag{3.15}$$

$$\boldsymbol{\Delta\sigma}_{\parallel}^{*} = \min_{-\sigma_{\parallel} \leq \Delta\sigma_{\parallel} \leq 0.01\sigma_{\parallel}} \left\| \begin{bmatrix} \boldsymbol{J}_{\parallel} \\ \alpha\boldsymbol{L} \end{bmatrix} \boldsymbol{\Delta\sigma}_{\parallel} - \begin{bmatrix} \boldsymbol{V}_{m} \\ \boldsymbol{0} \end{bmatrix} \right\|_{2}^{2} \tag{3.16}$$

$$\boldsymbol{\Delta\sigma}_{\perp}^{*} = \min_{-\sigma_{\perp} \leq \Delta\sigma_{\perp} \leq 0.01\sigma_{\perp}} \left\| \begin{bmatrix} \boldsymbol{J}_{\perp} \\ \alpha\boldsymbol{L} \end{bmatrix} \boldsymbol{\Delta\sigma}_{\perp} - \begin{bmatrix} \boldsymbol{V}_{m} \\ 0 \end{bmatrix} \right\|_{2}^{2} \tag{3.17}$$

In the absence of closed-form solutions, these 'directional' sensitivity matrices are numerically constructed via a two-point secant method using multiple solutions of the forward

problem. For example, as shown in equation (3.18), the in-plane sensitivity matrix is assembled column-wise by the numerical difference of voltage vectors with slight perturbation of in-plane conductivity, $\delta\sigma^e$, at the eth element of the domain. The Jacobian with respect to through-thickness direction is constructed in a similar manner as shown in equation (3.19). $\boldsymbol{J}_{\parallel}^e$ and $\boldsymbol{J}_{\perp}^e$ represent the eth column of the directional sensitivity matrix where e goes up to the total number of elements in the EIT reconstruction mesh.

$$\boldsymbol{J}_{\parallel}^e = \frac{\boldsymbol{F}(\boldsymbol{\sigma}_{\parallel} + \delta\sigma^e) - \boldsymbol{F}(\boldsymbol{\sigma}_{\parallel} - \delta\sigma^e)}{2\delta\sigma^e} \tag{3.18}$$

$$\boldsymbol{J}_{\perp}^e = \frac{\boldsymbol{F}(\boldsymbol{\sigma}_{\perp} + \delta\sigma^e) - \boldsymbol{F}(\boldsymbol{\sigma}_{\perp} - \delta\sigma^e)}{2\delta\sigma^e} \tag{3.19}$$

4. EXPERIMENTAL PROCEDURE

This chapter provides an overview of the manufacturing and experimental techniques used in this work.

4.1 Manufacturing

Two types of CFRP specimens were produced – planar square specimens and non-planar specimens. Both specimens used the same materials.

4.1.1 Planar Square Plate Specimens

Planar square plate specimens were produced for two purposes. First, these specimens were cut up into small squares such that in-plane and through-thickness conductivity measurements could be collected. And second, planar square plates were used for preliminary EIT testing before proceeding to non-planar specimens for EIT. The composite laminates in this study were manufactured using a combination of plain weave carbon fibre fabric and epoxy resin matrix (Fiber Glast 2000 series). Epoxy and hardener were mixed at a ratio of 100:25 by weight per the manufacturer's instructions. This was followed by the addition of BYK air release agent. Air release agent helps reduce the occurrence of bubbles and voids in the final composite. The mixture was gently stirred by hand for five minutes and then degassed for 30 minutes under vacuum at 0.1 MPa below atmospheric pressure and at room temperature. 15 layers of the fabric were stacked using the wet-layup technique where each layer was impregnated with the resin mixture using an applicator brush and squeegee before placing another fabric layer on top. The entire setup was vacuum bagged and cured under vacuum at 60 °C for five hours. A single cured laminate was then cut to 4.25"× 4.25" for EIT testing purposes. The $[0/90]_{15}$ layup sequence gives rise to orthotropic conductivity.

Additional plates were made in an identical fashion (Figure (4.1)) and cut up into small squares approximately measuring 0.5" × 0.5" such that the average in-plane and through-thickness conductivity could be measured and the orthotropic conductivity verified. To do this, conductive silver paint followed by copper strips was applied to these squares on faces
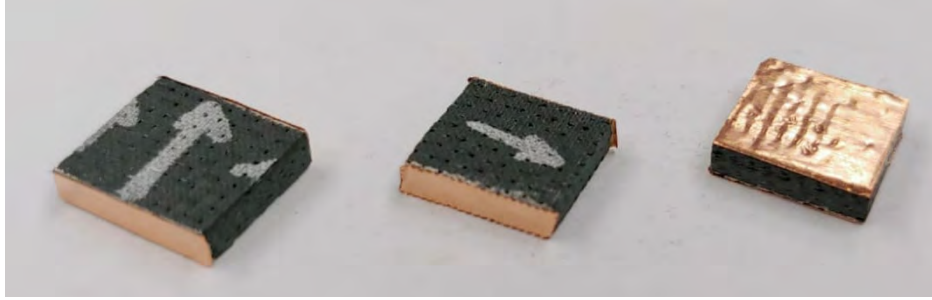
Figure 4.1. Resistance measured in both in-plane and through-thickness directions.

perpendicular to the direction in which resistance was to be measured. Resistances were measured using a hand-held digital multi-meter (DMM). Conductivity was then calculated based on the resistance measurements and the specimen dimensions. Average in-plane and through-thickness conductivities are shown in Table (4.1). A total of 47 small squares were tested this way. These averages were used to gauge the range of conductivity values to consider when estimating the baseline conductivity of a specimen as discussed at the end of this chapter.

Table 4.1.
Conductivity estimate of samples as measured in principal directions.

Direction	Average
$\sigma_{\parallel}$	5906±1121 S/m
$\sigma_{\perp}$	294±125 S/m

4.1.2 Non-Planar Airfoil Specimen

In order to test the proposed approach on shapes with greater geometric complexity than flat plates, non-planar laminates were also made. For this, laminates were made in the shape of NACA airfoils. Note that the airfoil shape is not meant to represent any particular structural application. Rather, it was merely chosen as a representative non-planar shape of significance to aerospace. For this, a female aluminium mold in the shape of the upper surface of a NACA 4424 airfoil was milled as shown in the Figure (4.2).
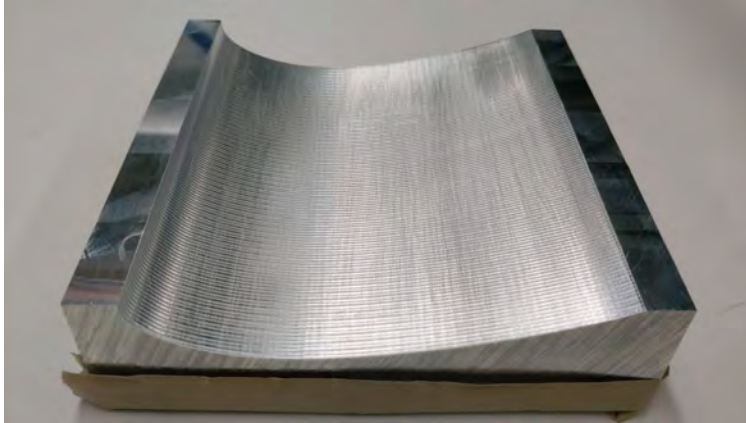
Figure 4.2. Aluminum mold used to prepare non-planar composite test specimens.

A similar manufacturing procedure was carried out to prepare non-planar airfoil composites using the same raw material – wet layup was used with the female mold as a base. However, to ensure that the specimens were completely cured, they were placed under vacuum for an hour longer (six hours in total) at a slightly higher temperature of 70 °C. Once cured, the edges of the composite were cut down to the desired dimensions. An airfoil of 5" in chord length and 4" in width produced this way can be seen in Figure (4.3).

Figure 4.3. A cured airfoil specimen used for testing. This airfoil is 4" in width with a chord length of 5."

4.2 EIT Injection Patterns

Traditional EIT with edge-mounted electrodes often makes use of an adjacent injection pattern wherein current is injected between adjacent electrode pairs and voltages are likewise measured between adjacent electrodes. This is schematically illustrated in Figure 4.5 (a). Herein, however, recall that we are interested in surface-mounted electrodes; specifically, electrodes uniformly distributed over the entire surface of the domain. For such a case, there is no direct equivalent to an adjacent injection pattern. Hence, two patterns were considered – a 'snake-like' pattern and a 'spiral' pattern. Both of these are schematically illustrated in Figures 4.5 (b) and (c). Because an in-depth investigation of optimal injection patterns is beyond the scope of this thesis, the ranks of the sensitivity matrices were compared. This analysis was done computationally using the forward model described previously, and it was found that both patterns generated sensitivity matrices of the same rank. Hence, 'snake-like' pattern was picked merely based on it providing qualitatively superior images during computational testing. SVD plots of this analysis can be seen in Figure (4.4).
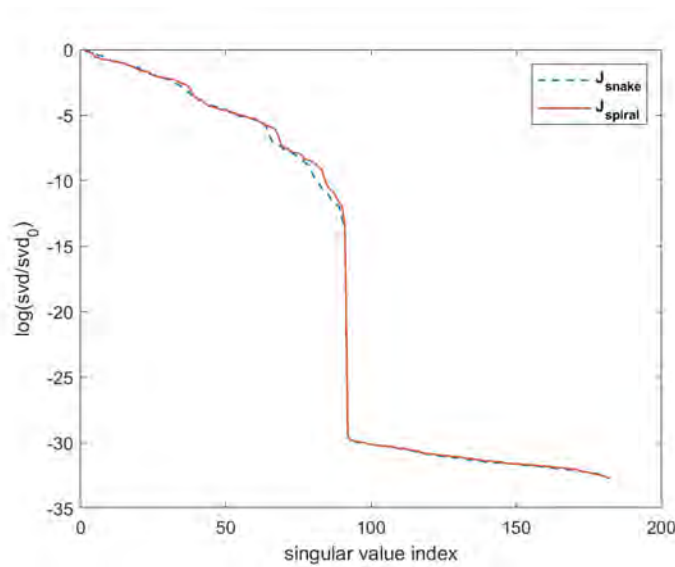
Figure 4.4. Rank comparison of 'snake-like' and 'spiral' current injection patterns.
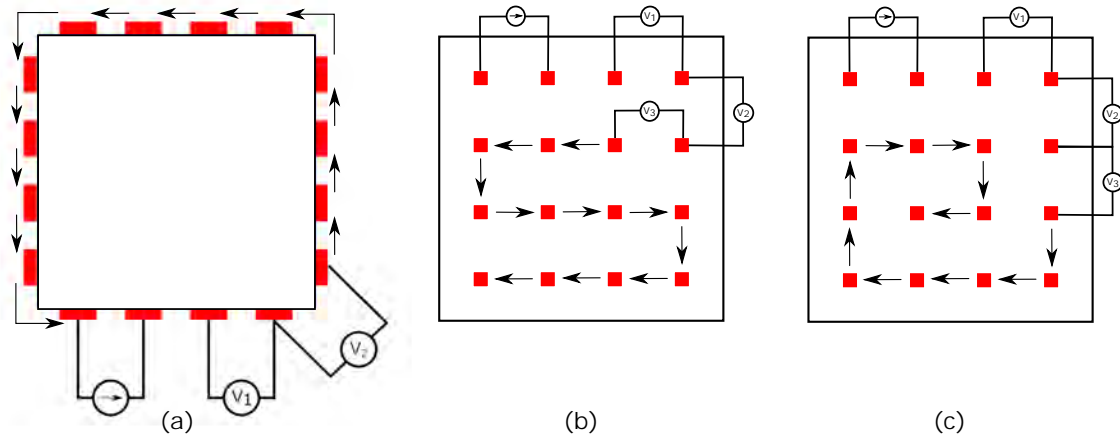
Figure 4.5. Schematic representation of (a) edge-mounted electrodes with adjacent injection pattern and surface mounted electrodes with (b) 'snake-like' and (c) 'spiral' injection pattern.

4.2.1 Planar Square Specimen

For preliminary testing on the square planar specimen, a total of 16 electrodes were painted equidistant to one another as 0.25" squares over the surface of the specimen using highly conductive silver paint. Copper tape was then applied onto these electrode surfaces with extended tabs folded over the acrylic strips (i.e. electrode bars) as shown in Figure (4.6) for ease of connection to leads with alligator clips.

4.2.2 Airfoil Specimen

For the airfoil specimens, due to a larger upper-surface area available than on the planar square plate, 20 electrodes were painted in a similar fashion. Instead of relying on copper tape, silver paint was directly applied to the acrylic strips that were placed over these electrodes. This helps to extend the electric connectivity to the alligator leads clipped on during testing. This is shown in Figure (4.7). This setup proved to offer more stable measurements for better quality reconstructions since applied copper tapes could possibly detach from the electrode surface mid-experiment leading to errors in measurements.
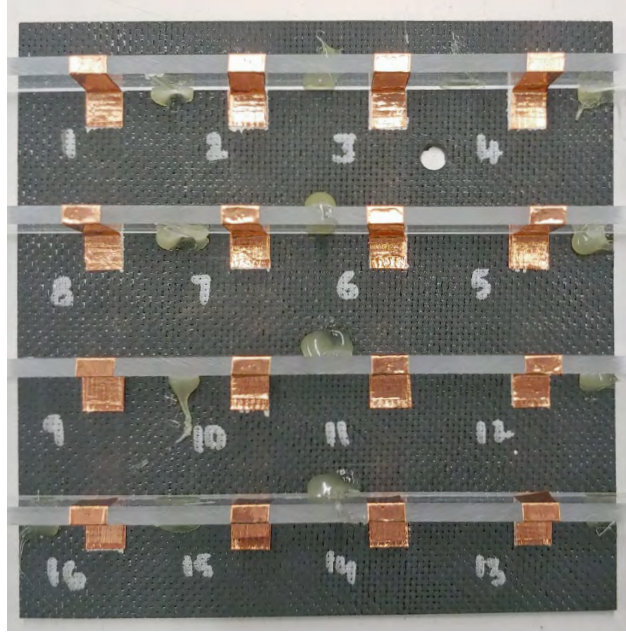
Figure 4.6. CFRP planar specimen with attached electrodes. Note: Hot glue used to hold the electrode bars in place.
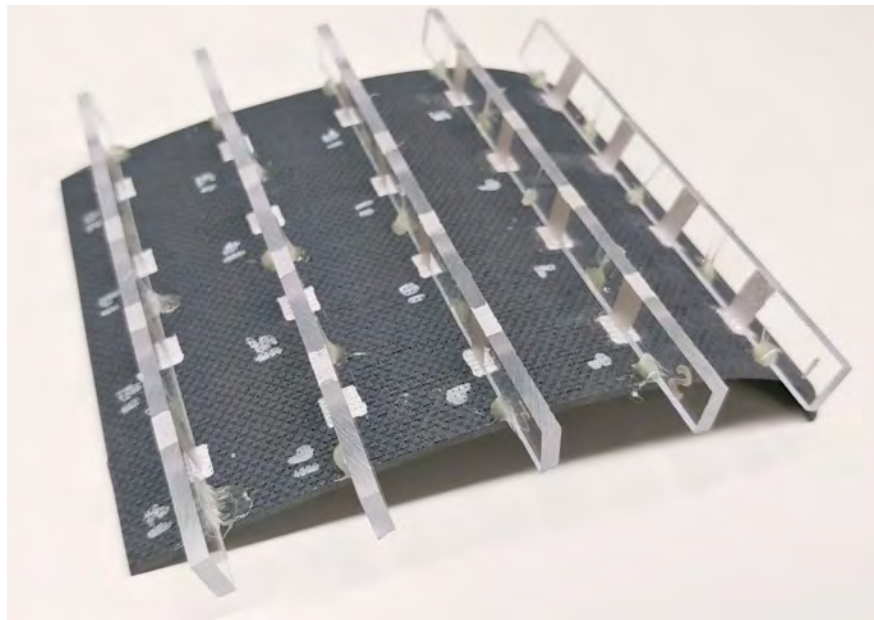
Figure 4.7. Airfoil specimen with painted electrodes.
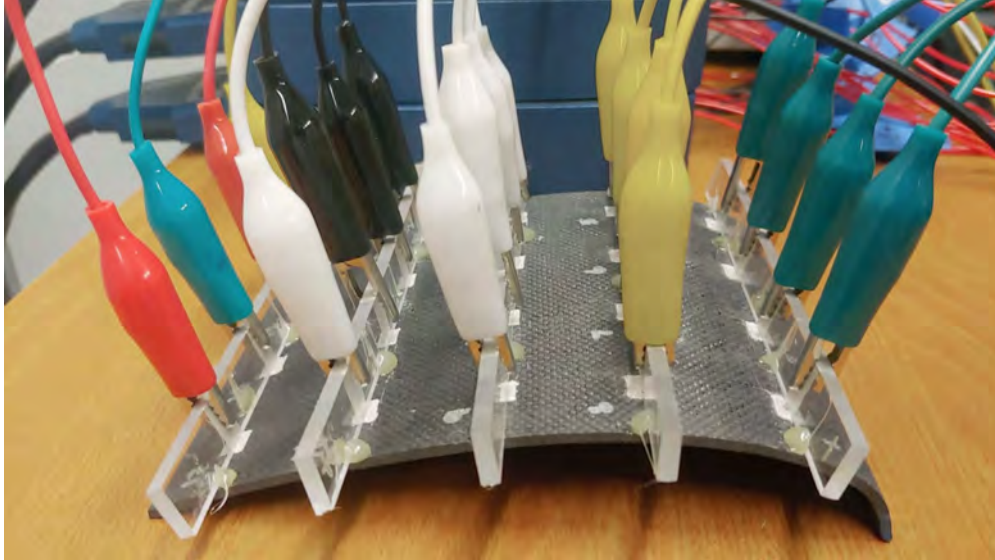
Figure 4.8. Specimen setup with attached leads for testing.

4.3 Procedural Details

A constant DC was used in this work. The current amplitude was selected to remain within the voltage range of the data acquisition (DAQ) system while also maximizing the measured inter-electrode voltages. Thus, the current magnitude for each specimen was picked such that output voltage of all electrodes on a current injection fall under the 10 V limit set by the DAQ. Since the same current magnitude needs to be supplied at each stage of the experiment (i.e. before and after damage) a value safely lower than the maximum usable amperage was chosen in order to account for increases in resistance between electrodes due to damage.

Once the voltages are measured pre-damage, the baseline conductivity, $\boldsymbol{\sigma}_{ij}$, for the domain can be set. This requires the generation of predicted voltage vectors for a range of baseline conductivities as described in the forward problem. The l_2 error norms between these predicted voltages and the pre-damage experimental voltage vector are then compared. The conductivity estimate that generates the lowest error value is set as the baseline conductivity for the specimen. An example of the baseline conductivity tensor, σ_{ij}, chosen for a DC supply of 0.3 A for the planar specimen used in this study is as shown in equation (4.1). Here, $\sigma_{\parallel} = \sigma_{11} = \sigma_{22}$ and $\sigma_{\perp} = \sigma_{33}$ respectively represent the in-plane and through-thickness

baseline conductivity values. The predicted voltage vector generated using these values show good agreement with the voltage measurements obtained from the EIT experiment as seen in Figure (4.9). This estimate is also in relatively good agreement with the measured averaged shown in Table (4.1).

$$
\sigma_{ij} = \begin{bmatrix} 5900 & 0 & 0 \\ 0 & 5900 & 0 \\ 0 & 0 & 390 \end{bmatrix} \text{S/m}
\tag{4.1}
$$
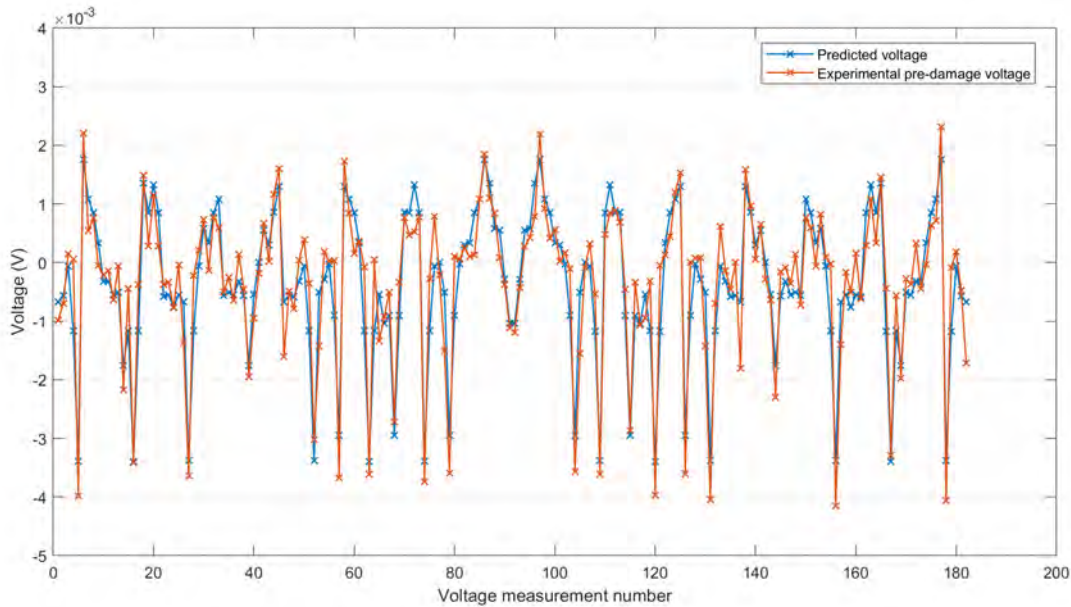
Figure 4.9. A graphical comparison of the pre-damage voltage data collected from the planar specimen, and the forward predicted voltages for the baseline conductivity mentioned in equation (4.1).

For all the tested specimens, current was injected by a BK Precision 9131B power supply and voltages were measured using National Instruments PXIe-6368 DAQ cards at a frequency of 100 Hz. For every current injection, data was collected from each electrode with respect to ground for 10 seconds so that averages could be used in EIT calculations. This helps minimize the effect of noise. Inter-electrode voltages were calculated offline.

5. EXPERIMENTAL RESULTS

5.1 Through-Hole Damage Reconstruction in Planar Specimen

Preliminary experimental work concerned detecting a single through-hole damage in a square CFRP plate. This was done in order to verify that the surface-mounted electrode array worked on a simpler geometry before progressing to the non-planar case. After collecting pre-damage voltages from the plate using the 'snake-like' injection pattern described previously, a 3/16" hole was drilled in the upper right-hand side of the plate. The post-damaged plate is shown in Figure (4.6). After this, post-damage voltages were measured. In the forthcoming, two sets of results are presented. The first being the effect of sensitivity matrix formulation on sensitivity matrix rank as assessed by SVD. And second, the effect of these formulations on the through-hole detection.

Figure (5.1) shows the logarithm of the normalized singular values of $\boldsymbol{J}^{\kappa}$, $\boldsymbol{J}_{\parallel}$ and $\boldsymbol{J}_{\perp}$ plotted against singular value number. In EIT, the quality of reconstruction can be linked to the rank of the sensitivity matrix. Higher ranks generally provide better imaging capabilities. As seen in Figure (5.1), all sensitivity values drop at the same index value in the plot, which confirms that the different formulations do not lead to a loss in the rank of the sensitivity matrix. This means that no information is lost to the inverse problem through this approach.
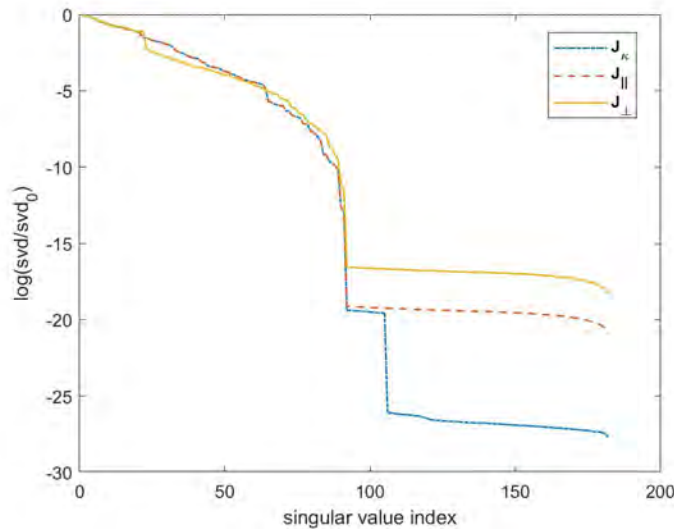
Figure 5.1. Rank assessment of the three sensitivity matrices via SVD.
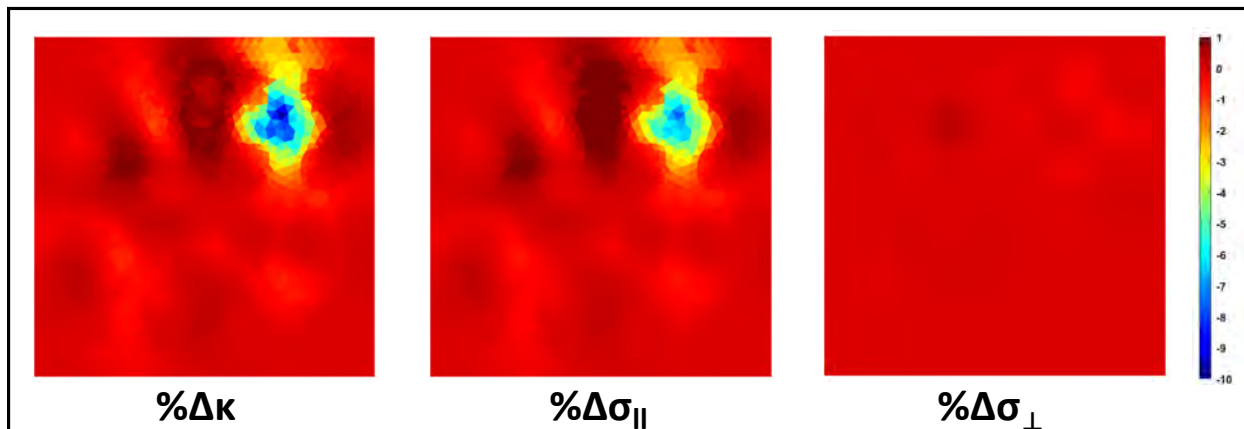
Figure 5.2. EIT reconstructions of through-hole damage in flat plate plotted as percentage change in $\Delta\boldsymbol{\kappa}$ and $\Delta\boldsymbol{\sigma}_\parallel$ and $\Delta\boldsymbol{\sigma}_\perp$.

Following the SVD analysis, we look at the image reconstructions in Figure (5.2). We notice that damage is clearly detected in the case of sensitivity matrix formulations with respect to $\boldsymbol{\kappa}$ and with respect to $\boldsymbol{\sigma}_\parallel$ but not with respect to $\boldsymbol{\sigma}_\perp$. These results suggest that both $\boldsymbol{\kappa}$ and $\boldsymbol{\sigma}_\parallel$ are sensitive to this type of damage while $\boldsymbol{\sigma}_\perp$ is not. To better understand this, we recall that in the case of CFRPs, it is the carbon fibres that form the conductive pathways. Based on the fibre layup in the laminate used in this study, the conductivity in the in-plane direction is much higher. It is therefore easier for current to flow along these fibres than in the through-thickness direction that owes its conductivity only to inter-laminar fibre contact. This can be confirmed by the baseline conductivity recorded in Table (4.1). Additionally, inter-electrode transport is much more dependent on in-plane conductivity. Hence, with respect to a through-hole damage, we find that the Jacobian is largely influenced by the severe decrease in in-plane conductivity due to the lack of conductive network of fibres in the damaged region as compared to the smaller inter-laminar loss, rendering it unable to detect the damage by the sensitivity matrix formulation with respect to $\boldsymbol{\sigma}_\perp$.

5.2 Through-Hole Damage Reconstruction in Non-Planar Airfoil

Having confirmed that the different sensitivity matrix formulations presented in this study yield good results when tested on a planar specimen, in this subsection we shall take a look at how this applies to curved structures similar to those seen in real-life applications.

50

For a curved airfoil structure as shown in the Figure (5.3), multiple holes of varying sizes were drilled at different locations. The first hole of 1/8" was drilled at location 1 followed by boring it out to 1/4" diameter while EIT measurements were collected at both instances. Similarly, holes of 1/8" and subsequently 1/4" were drilled at positions 2 and 3. Between all the holes and all the hole sizes, a total of six post-damage EIT data sets were collected from the airfoil.
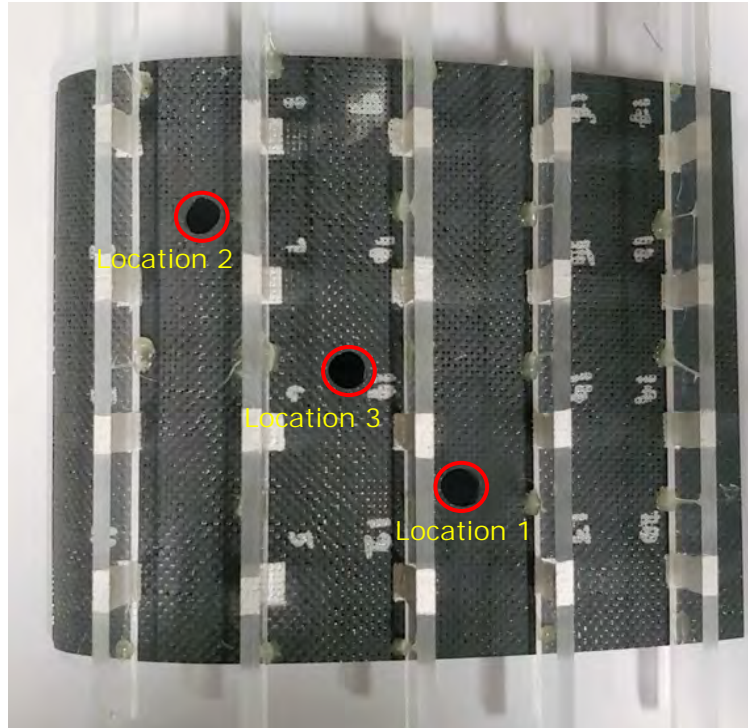
Figure 5.3. The location of drilled holes are marked in red. At each location 1/8" hole was initially drilled and then enlarged to 1/4" diameter before moving to the next location.

The EIT results for the sensitivity matrix formulations with respect to $\boldsymbol{\kappa}$, $\boldsymbol{\sigma}_\parallel$ and $\boldsymbol{\sigma}_\perp$ for all steps of damage are presented in Figure (5.4). Here, each row displays the results obtained on a particular state of damage. Each damage is scaled to show a percentage change in $\boldsymbol{\kappa}$, $\boldsymbol{\sigma}_\parallel$ and $\boldsymbol{\sigma}_\perp$. Since the airfoils use the same material system with similar conductive properties as the square plate, we see similar quality of damage reconstructions from each type of formulation. And as was also observed for the plates, the damage was detected in

the cases of sensitivity matrix formulations with respect to $\boldsymbol{\kappa}$ and with respect to $\boldsymbol{\sigma}_{\parallel}$, but not with respect to $\boldsymbol{\sigma}_{\perp}$.
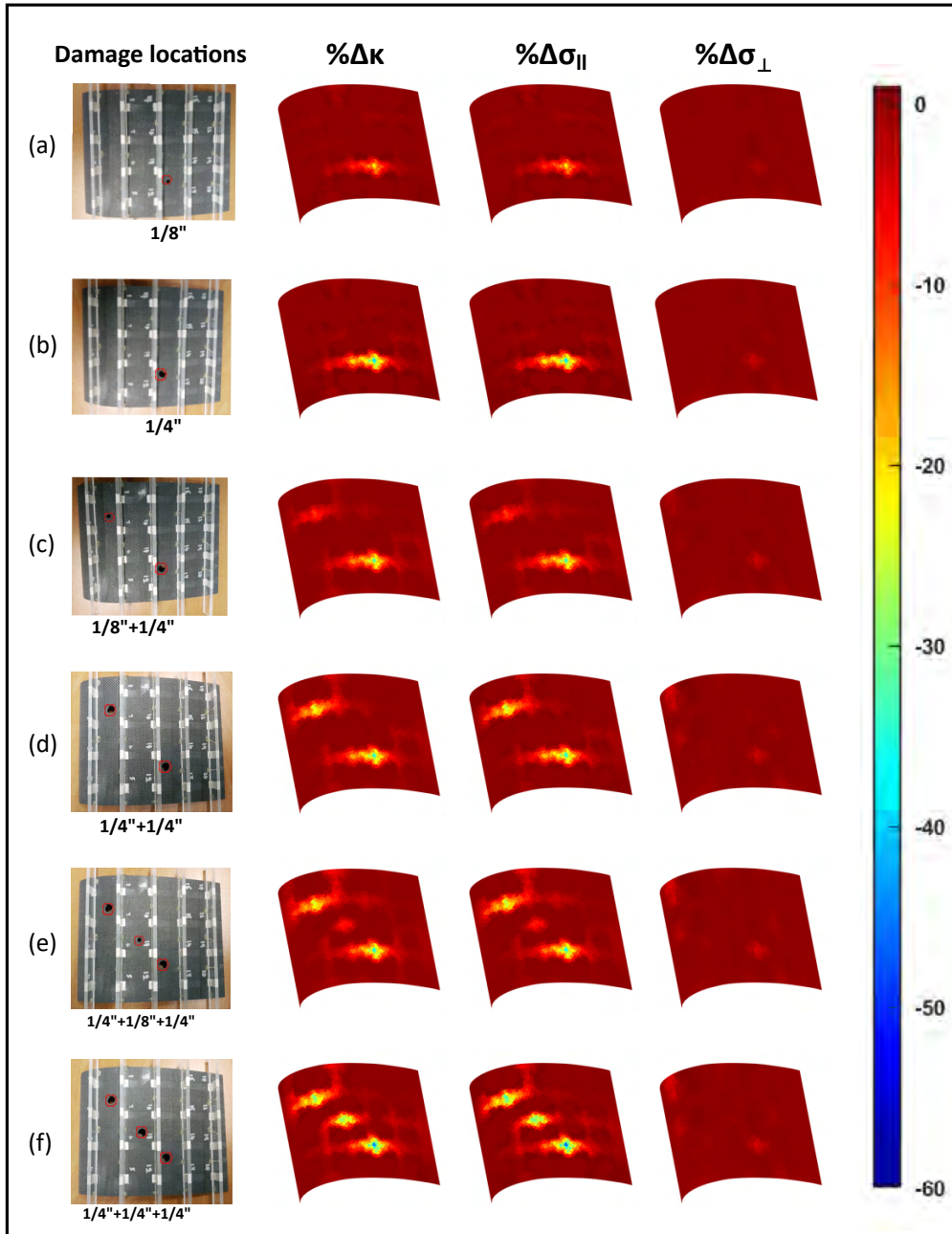
Figure 5.4. EIT reconstructions of conductivity distribution with respect to $\boldsymbol{\Delta\kappa}$, $\boldsymbol{\Delta\sigma}_{\parallel}$ and $\boldsymbol{\Delta\sigma}_{\perp}$. Results are presented as a percent change from the pristine baseline value.

Looking at the overall results, we notice every new damage could be successfully detected. Furthermore, compared to the pristine estimated in-plane conductivity of $\boldsymbol{\sigma}_\parallel = 5500$ S/m, there seems to be a maximum conductivity decrease of roughly 50% for the largest holes. The same can be observed for the decrease in $\boldsymbol{\kappa}$, where loss in its magnitude is directly related to the overall decrease of conductivity from its baseline magnitude, $\bar{\boldsymbol{\sigma}}_{ij}$.

On comparing each row, we can also notice that there is a lower percentage change in conductivity magnitude for every new damage introduced. For example, on comparing the 1/8" hole drilled at location 1 (row(a)) to the damage reconstructed for the same sized hole drilled at location 2 (row (c)), we notice a lower change in conductivity (both with respect to $\boldsymbol{\kappa}$ and $\boldsymbol{\sigma}_\parallel$), making it comparatively less visible. However, if the damage state shown in Figure 5.4 (b) is chosen as the baseline to detect the 1/8" hole at location 2, the damage becomes clearly visible. This indicates that new damages are overshadowed by the presence of older damages but they can be recovered using a different baseline. As for the results obtained with sensitivity matrix formulated with respect to $\boldsymbol{\sigma}_\perp$, we notice that no damage could be detected owing to the lesser conductivity of the structure in the through-thickness direction.
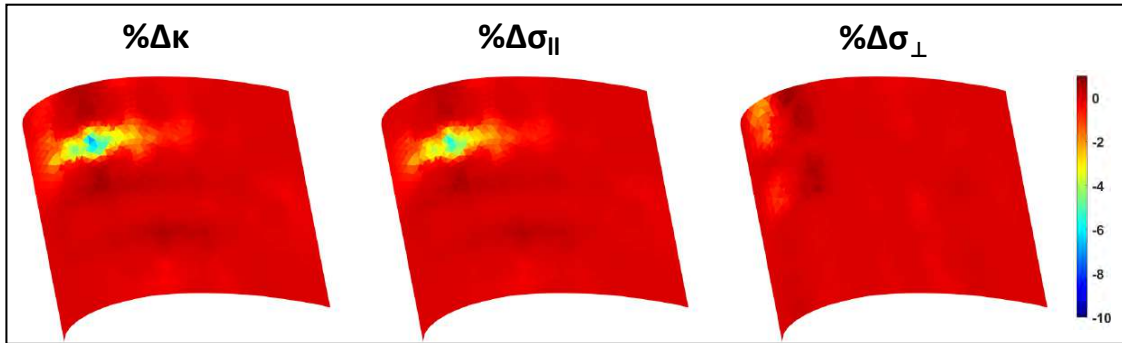
Figure 5.5. EIT reconstructions of 1/8" hole at location 2 with Figure (5.4)(b) chosen as the baseline.

For completeness, the normalized singular values of the three Jacobians formulated for this experiment are again plotted against their singular value indices in Figure (5.6). As was the case for the square planar plate, it can be observed that sensitivity matrix formulation does not seem to impact the rank of the sensitivity matrix.
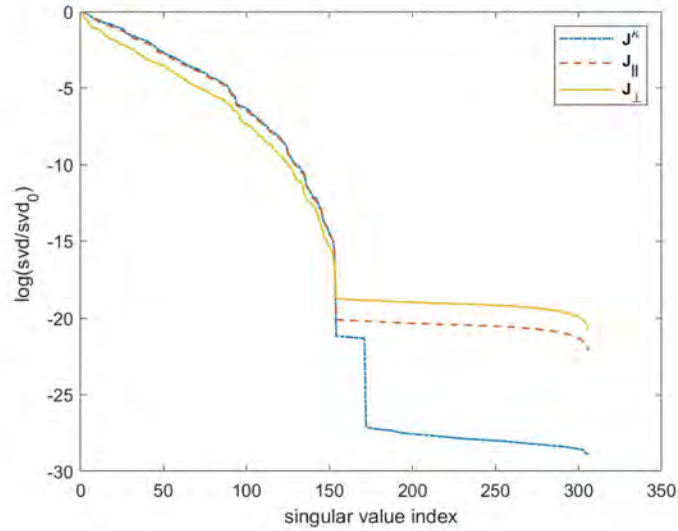
Figure 5.6. Rank assessment of the three sensitivity matrices via singular value decomposition for non-planar airfoil subject to through-hole damage.

5.3   Impact Damage Reconstruction in Non-Planar Airfoil

Even though through-hole testing provides a useful benchmark, through-hole damages are obviously not representative of real damages typically incurred by composites. Therefore, we shall now look at damage detection results due to impact tests on a curved airfoil specimen. The impact tests were conducted using a CEAST 9340 drop tower. Since the testing rig was originally designed to fit only planar specimens, the aluminium mold was used as a fixture to place the specimen on while testing. Left unsupported, the specimen would merely collapse upon impact which would be an unambiguous case of damage. Using a semi-rigid backing also helps to isolate the damage to the vicinity of the impact. Due to using a female mold in the manufacturing process, the specimen would have to be impacted at the bottom surface instead of the top surface (a top-surface impact would be more likely for actual in-service structures). Importantly, however, this change in surface does not alter the modes of damages encountered post-impact and hence is an acceptable setup to demonstrate proof-of-concept. As shown in Figure (5.7), the specimen is laid upside down on the mold and C-clamps are placed around the specimen to restrict movement.
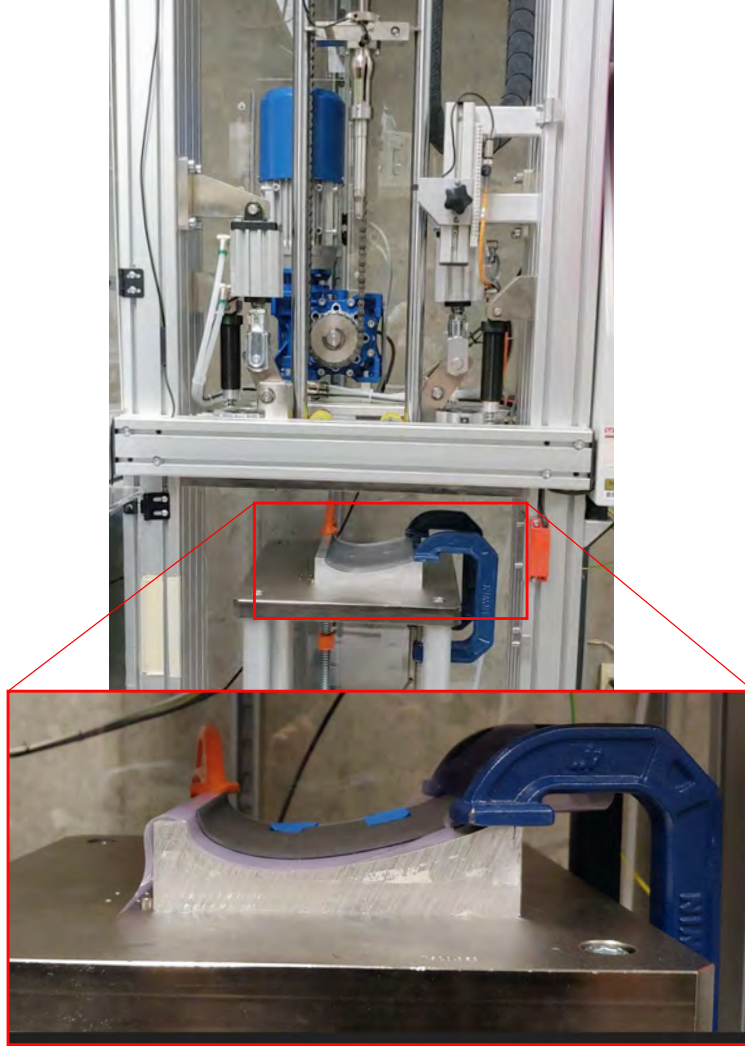
Figure 5.7. The airfoil specimen is placed upside down on the aluminium mold to be impacted.

The specimen was first impacted with 15 J of energy followed by a second 12 J impact. These impacts were done at different locations on the airfoil as shown in Figure (5.8). Based on simple visual inspection of the impacted surface, the larger energy of 15 J results in a greater degree of damage as expected, while the impact of 12 J left a mere indentation at the location without significantly visible surface alteration. Figure (5.9) is provided for a closer look at the cracks caused on the upper surface of the specimen due to the 15 J impact.

EIT results obtained for all three sensitivity matrices are shown in Figure (5.10). We immediately notice that the first impact of 15 J (corresponding to the top row of this figure)
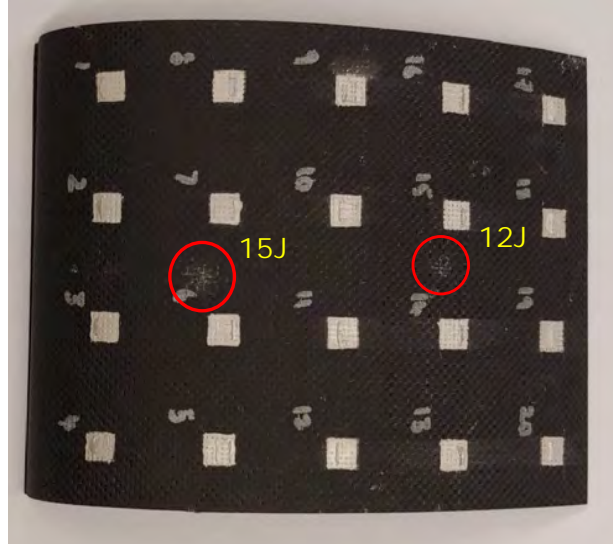
(a) Top View
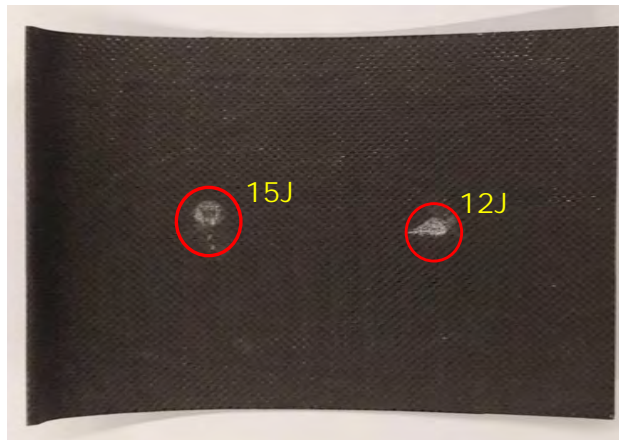
(b) Bottom View (Point of Impact)

Figure 5.8. (a) Top view and (b) bottom view of the post-impacted airfoil with the impacted regions circled in red.

is clearly visible for reconstructions corresponding to Jacobians with respect to $\boldsymbol{\kappa}$ and $\boldsymbol{\sigma}_\parallel$. The second impact damage of 12 J energy, however, does not yield as significant a change in conductivity as the previous higher-energy impact. Nonetheless, the second impact is still clearly visible. It stands to reason that a lower-energy impact caused less damage and therefore effected less conductivity change in the CFRP. However, we must note that unlike the reconstructions shown in the previous section with through-hole damage testing, there exist mild artifacts in the form of lighter shades of red on the surface. These sections of the structure have not undergone any damage. It is therefore speculated that due to the
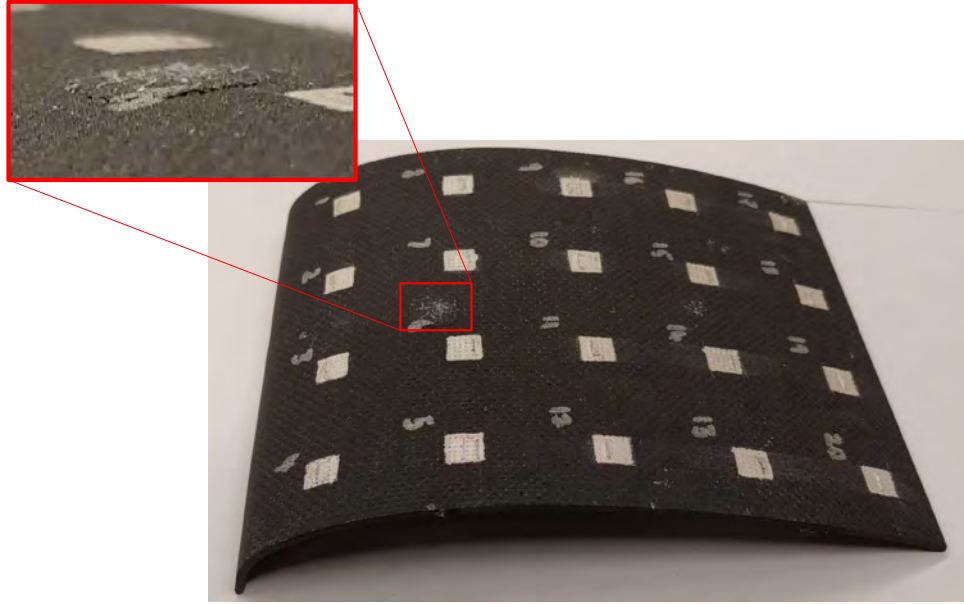
Figure 5.9. Enlarged image of the upper surface damage caused by an impact of 15 J.

removal and subsequent replacement of the acrylic strips used for experimentation, mild errors in voltage measurements might have been caused, thus, emerging as artifacts.

Lastly, to ensure that the second impact is still clearly detectable, a second set of EIT images were formed using the 15 J damage case as the baseline for difference imaging (as opposed to the undamaged case). These results are shown in Figure (5.11). From this, despite the mild artifacts, we clearly notice the damage caused by the lower energy impact resulting in roughly 10% decrease with respect to $\boldsymbol{\kappa}$ and $\boldsymbol{\sigma}_{\parallel}$. This confirms that the lower-energy impacts are still clearly visible, just overshadowed by the higher-energy impacts when formed using a pristine baseline. The rank of these sensitivity matrices is also plotted in Figure (5.12). As expected, the different sensitivity matrices have the same rank.

If we were to compare the conductivity loss due to damage in these impact tests versus that seen in through-hole damages, we notice that the conductivity change in the former case is relatively low. This can be attributed to the fact that unlike a through hole damage where the conductive fibre link disappears completely at a location, an impact damage leads to a milder case of fibre breakage and/or delamination. Hence, we see only a 30% decrease in conductivity change versus a 50% loss in case of through-hole damages. Although a rigorous
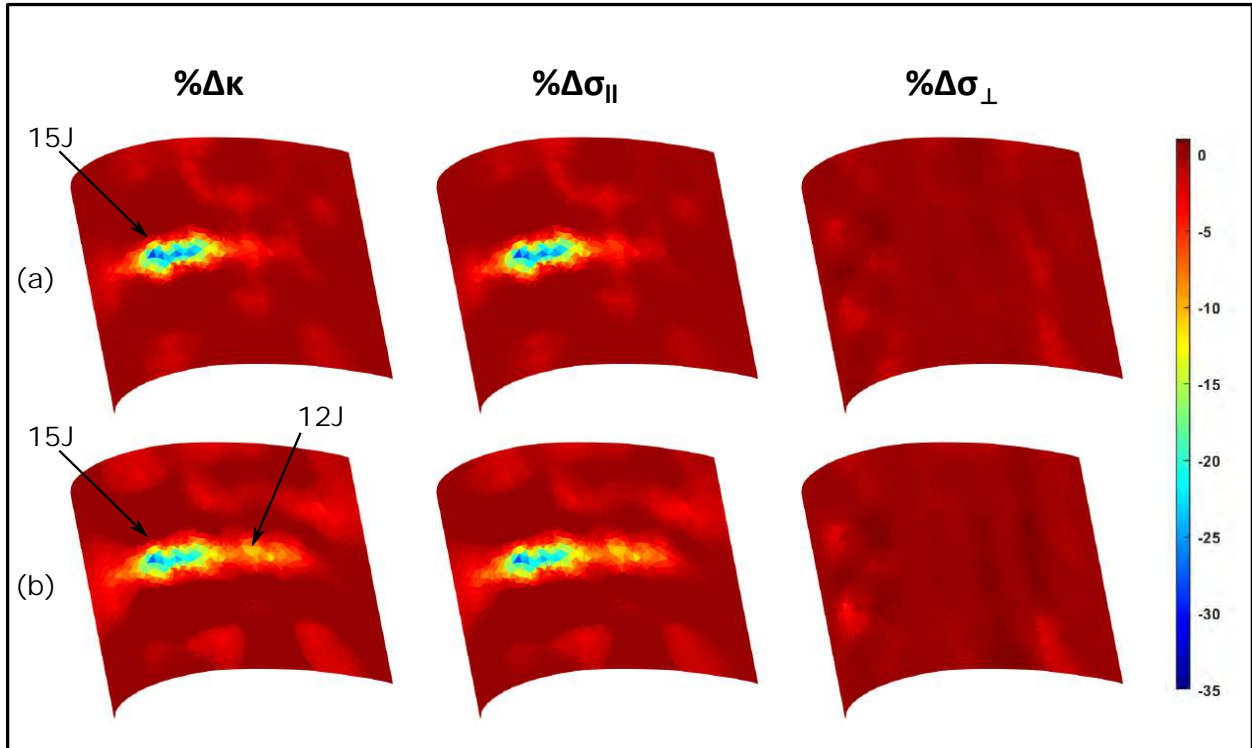
Figure 5.10. EIT reconstruction of (a) just the 15 J impact and (b) both the original 15 J and the subsequent 12 J impact (recall the impacts were at different locations) with respect to $\%\boldsymbol{\Delta\kappa}$, $\%\boldsymbol{\Delta\sigma}_{\parallel}$ and $\%\boldsymbol{\Delta\sigma}_{\perp}$.
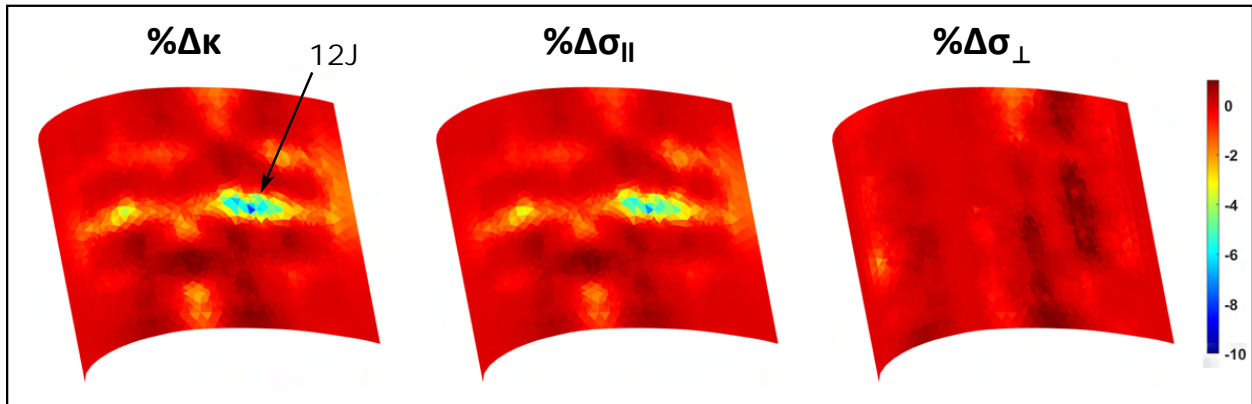
Figure 5.11. EIT reconstruction of the 12 J impact with 15 J damage case as baseline. The 12 J impact is now much more visible for the first two formations of the sensitivity matrix.

destructive evaluation of the post-impacted plates exceeds the scope of this thesis, some elementary optical microscopy was conducted in order to confirm the existence of broken
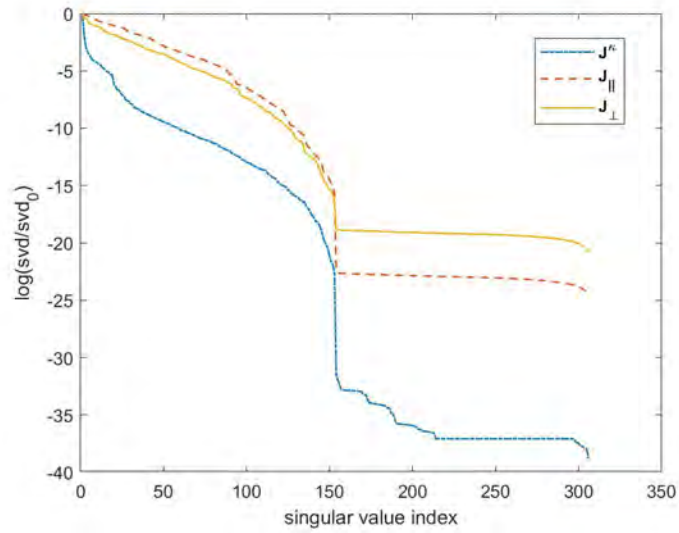
Figure 5.12. Rank assessment of the three Jacobians formulated for impact testing.

carbon fibres at the impact location. For this, the post-impacted airfoil was cut at the impact location and then imaged using a Zeiss Axioskope 2 optical microscope. Shown in Figure (5.13), fibre breakage is clearly seen. This confirms the mechanism of conductivity change in the CFRP.

Figure 5.13. Fibre breakage (circled) seen along the cross-section at impacted site.

6. SUMMARY AND CONCLUSIONS

This study set out to broaden the potential of EIT for damage detection in CFRPs. To reiterate, the growing popularity of composites, particularly CFRPs for industrial and transportation applications demands an equally capable inspection technique. With the limitations of current modes of SHM, and the comparative lack of literature on EIT specific to CFRPs, this research hopes to meaningfully contribute to the state of the art by addressing the challenges involved in terms of complex non-planar geometries and anisotropic conductive properties.

To that end, a brief explanation of the mathematical framework was provided with the minimization of voltage measurements conducted using three different sensitivity matrix formulations. These were namely with respect to a scalar multiplier of the conductivity tensor ($\boldsymbol{\kappa}$), with respect to conductivity estimate in both in-plane ($\boldsymbol{\sigma}_{\parallel}$) and through-thickness ($\boldsymbol{\sigma}_{\perp}$) directions. An experimental setup with surface-mounted electrodes was discussed due to the inaccessibility of edges in most engineering structures. Three sets of experiments were conducted: First, a preliminary EIT experiment was conducted by inducing a single through-hole damage in a simple CFRP plate in order to assess the feasibility of using surface-mounted electrodes. Following the success of this preliminary study, EIT was used to detect through-hole as well as impact damage in non-planar airfoil-shaped laminates.

The results presented in this thesis work show that sensitivity matrix formulations play a role in addressing the anisotropy of a composite structure. It is seen that the damage (both through-hole and impact kind) are detected with a sensitivity matrix formulation with respect to $\boldsymbol{\kappa}$. In regards to the direction dependent sensitivity matrices $\boldsymbol{J}_{\parallel}$ and $\boldsymbol{J}_{\perp}$, the damages are detected with respect to the in-plane conductivity with qualitatively the same level of accuracy as with respect to the scalar multiplier.

Since fibres act as the conductive medium in CFRPs, the bi-directional placement of these continuous fibres in our specimen leads to greater conductivity in the in-plane direction. The existence of through-thickness conductivity is a consequence of inter-laminar fibre contact, which is much lower in magnitude. Therefore, we believe it is the larger loss in conductivity due to breakage of these fibres in the in-plane direction that conceals the loss in conductivity due to the absence of inter-laminar fibre contact in the through-thickness

direction in the region of damage. This leads to comparatively poor damage reconstructions when conductivity is mapped in the through-thickness direction. However, other material systems with higher through-thickness conductivity may actually be better imaged using the through-thickness sensitivity matrix. But more work is needed to confirm this.

In conclusion, this thesis looked to address the key present-day challenges in applying EIT to non-planar CFRP composites. To that end, two notable contributions were made. Firstly, modification to the mathematical formulation of EIT inverse problem was implemented in terms of directionally dependent sensitivity matrices in addition to the already existing scalar multiplier of the conductivity tensor. While the effectiveness of $\boldsymbol{J}^{\kappa}$ and $\boldsymbol{J}_{\parallel}$ were confirmed through the EIT reconstructions, $\boldsymbol{J}_{\perp}$ would require further testing for a different CFRP layup. Secondly, the proposed surface-mounted electrodes demonstrated satisfactory performance with regard to damage detection and localization. This is an important step away from the edge-mounted electrodes traditionally used in EIT.

6.1 Recommendations for Future Work

While this thesis outlines a method for successful damage detection in CFRPs using EIT, there is still a long way to go before actually implementing this for real in-service structures. Therefore, below are a few suggestions by the author for future work.

1. The preliminary work presented here needs to be expanded to more complex geometries of greater electrical anisotropy (i.e. uni-directional CFRPs) to mimic those seen in real life applications. More testing is required to confirm if the proposed sensitivity matrix formulations can help distinguish between different modes of damage such a delaminations and fibre breakage in these conditions.

2. While it is acceptable to use acrylic electrode bars in testing to determine the viability of a concept, electrode integration in a practical setting would require greater study into building slim electrodes that are well protected and robust enough to survive harsh environmental conditions.

3. In this study, we qualitatively compared just two injection patterns for surface-mounted electrodes. Therefore, a deeper study on the various possible current injection and voltage measurement schemes is required to definitively prove what works best.

4. While we have been able to localize damages in our case, the precise shape and size of these damages cannot be easily inferred from the EIT reconstructions. Hence, research could be undertaken (based on recent publications [84]) to probably incorporate direction dependent conductivity changes in metaheuristic algorithms to determine the underlying damage mechanism in anisotropic CFRPs.

REFERENCES

[1] W. Cantwell and J. Morton, "The significance of damage and defects and their detection in composite materials: A review," *The journal of strain analysis for engineering design*, vol. 27, no. 1, pp. 29–42, 1992.

[2] H. Towsyfyan, A. Biguri, R. Boardman, and T. Blumensath, "Successes and challenges in non-destructive testing of aircraft composite structures," *Chinese Journal of Aeronautics*, vol. 33, no. 3, pp. 771–791, 2020.

[3] T. D'orazio, M. Leo, A. Distante, C. Guaragnella, V. Pianese, and G. Cavaccini, "Automatic ultrasonic inspection for internal defect detection in composite materials," *NDT & e International*, vol. 41, no. 2, pp. 145–154, 2008.

[4] P. Vaara and J. Leinonen, "Technology survey on ndt of carbon-fiber composites," 2012.

[5] Y.-K. Zhu, G.-Y. Tian, R.-S. Lu, and H. Zhang, "A review of optical ndt technologies," *Sensors*, vol. 11, no. 8, pp. 7773–7798, 2011.

[6] S. Pickering and D. Almond, "Matched excitation energy comparison of the pulse and lock-in thermography nde techniques," *Ndt & E International*, vol. 41, no. 7, pp. 501–509, 2008.

[7] M. E. Fitzpatrick and A. Lodini, *Analysis of residual stress by diffraction using neutron and synchrotron radiation*. CRC Press, 2003.

[8] S. Gholizadeh, "A review of non-destructive testing methods of composite materials," *Procedia Structural Integrity*, vol. 1, pp. 50–57, 2016.

[9] H.-Y. Kim, "Vibration-based damage identification using reconstructed frfs in composite structures," *Journal of Sound and Vibration*, vol. 259, no. 5, pp. 1131–1146, 2003.

[10] T. Ooijevaar, R. Loendersloot, L. Warnet, A. de Boer, and R. Akkerman, "Vibration based structural health monitoring of a composite t-beam," *Composite Structures*, vol. 92, no. 9, pp. 2007–2015, 2010.

[11] E. Manoach, S. Samborski, A. Mitura, and J. Warminski, "Vibration based damage detection in composite beams under temperature variations using poincaré maps," *International Journal of Mechanical Sciences*, vol. 62, no. 1, pp. 120–132, 2012.

[12] A. Herman, A. Orifici, and A. Mouritz, "Vibration modal analysis of defects in composite t-stiffened panels," *Composite Structures*, vol. 104, pp. 34–42, 2013.

[13] S. Keye, M. Rose, and D. Sachau, "Localizing delamination damages in aircraft panels from modal damping parameters," in *Proceedings of the 19th International Modal Analysis Conference (IMAC XIX), Kissimmee, Florida, USA*, 2001, pp. 412–417.

[14] A. Güemes, A. Fernandez-Lopez, A. R. Pozo, and J. Sierra-Pérez, "Structural health monitoring for advanced composite structures: A review," *Journal of Composites Science*, vol. 4, no. 1, p. 13, 2020.

[15] R. Ruzek, M. Kadlec, K. Tserpes, and E. Karachalios, "Monitoring of compressive behaviour of stiffened composite panels using embedded fibre optic and strain gauge sensors," *International Journal of Structural Integrity*, 2017.

[16] S. Masmoudi, A. El Mahi, and S. Turki, "Fatigue behaviour and structural health monitoring by acoustic emission of e-glass/epoxy laminates with piezoelectric implant," *Applied Acoustics*, vol. 108, pp. 50–58, 2016.

[17] N. Alexopoulos, C. Bartholome, P. Poulin, and Z. Marioli-Riga, "Structural health monitoring of glass fiber reinforced composites using embedded carbon nanotube (cnt) fibers," *Composites Science and Technology*, vol. 70, no. 2, pp. 260–271, 2010.

[18] V. Giurgiutiu and G. Santoni-Bottai, "Structural health monitoring of composite structures with piezoelectric-wafer active sensors," *AIAA journal*, vol. 49, no. 3, pp. 565–581, 2011.

[19] J. S. Vipperman, "Simultaneous qualitative health monitoring and adaptive piezoelectric sensoriactuation," *AIAA journal*, vol. 39, no. 9, pp. 1822–1825, 2001.

[20] Z. Chaudhry, F. Lalande, A. Ganino, C. Rogers, and J. Chung, "Monitoring the integrity of composite patch structural repair via piezoelectric actuators/sensors," in *36th structures, structural dynamics and materials conference*, 1995, p. 1074.

[21] D. G. Cole and R. L. Clark, "Adaptive compensation of piezoelectric sensoriactuators," *Journal of Intelligent Material Systems and Structures*, vol. 5, no. 5, pp. 665–672, 1994.

[22] C. P. De Vera and J. Güemes, "Embedded self-sensing piezoelectric for damage detection," *Journal of intelligent material systems and structures*, vol. 9, no. 11, pp. 876–882, 1998.

[23] X. Li, Z. Yang, H. Zhang, Z. Du, and X. Chen, "Crack growth sparse pursuit for wind turbine blade," *Smart materials and structures*, vol. 24, no. 1, p. 015 002, 2014.

[24] P. Cawley, "Structural health monitoring: Closing the gap between research and industrial deployment," *Structural Health Monitoring*, vol. 17, no. 5, pp. 1225–1244, 2018.

[25] V. Memmolo, E. Monaco, N. Boffa, L. Maio, and F. Ricci, "Guided wave propagation and scattering for structural health monitoring of stiffened composites," *Composite Structures*, vol. 184, pp. 568–580, 2018.

[26] M. Mitra and S. Gopalakrishnan, "Guided wave based structural health monitoring: A review," *Smart Materials and Structures*, vol. 25, no. 5, p. 053 001, 2016.

[27] M. Salmanpour, Z. Sharif Khodaei, and M. Aliabadi, "Guided wave temperature correction methods in structural health monitoring," *Journal of Intelligent Material Systems and Structures*, vol. 28, no. 5, pp. 604–618, 2017.

[28] X. Li, Z. Yang, and X. Chen, "Quantitative damage detection and sparse sensor array optimization of carbon fiber reinforced resin composite laminates for wind turbine blade structural health monitoring," *Sensors*, vol. 14, no. 4, pp. 7312–7331, 2014.

[29] C. Fischer and F. Arendts, "Electrical crack length measurement and the temperature dependence of the mode i fracture toughness of carbon fibre reinforced plastics," *Composites science and technology*, vol. 46, no. 4, pp. 319–323, 1993.

[30] A. Kaddour, F. Al-Salehi, S. Al-Hassani, and M. Hinton, "Electrical resistance measurement technique for detecting failure in cfrp materials at high strain rates," *Composites Science and Technology*, vol. 51, no. 3, pp. 377–385, 1994.

[31] P.-W. Chen and D. Chung, "Carbon fiber reinforced concrete as an intrinsically smart concrete for damage assessment during static and dynamic loading," *Materials Journal*, vol. 93, no. 4, pp. 341–350, 1996.

[32] X. Wang and D. Chung, "Sensing delamination in a carbon fiber polymer-matrix composite during fatigue by electrical resistance measurement," *Polymer Composites*, vol. 18, no. 6, pp. 692–700, 1997.

[33] P. Irving and C. Thiagarajan, "Fatigue damage characterization in carbon fibre composite materials using an electrical potential technique," *Smart materials and structures*, vol. 7, no. 4, p. 456, 1998.

[34] D.-C. Seo and J.-J. Lee, "Damage detection of cfrp laminates using electrical resistance measurement and neural network," *Composite structures*, vol. 47, no. 1-4, pp. 525–530, 1999.

[35] J. Abry, Y. Choi, A. Chateauminois, B. Dalloz, G. Giraud, and M. Salvia, "In-situ monitoring of damage in cfrp laminates by means of ac and dc measurements," *Composites Science and Technology*, vol. 61, no. 6, pp. 855–864, 2001.

[36] I. Weber and P. Schwartz, "Monitoring bending fatigue in carbon-fibre/epoxy composite strands: A comparison between mechanical and resistance techniques," *Composites Science and Technology*, vol. 61, no. 6, pp. 849–853, 2001.

[37] J. Han, J. Pan, J. Cai, and X. Li, "A review on carbon-based self-sensing cementitious composites," *Construction and Building Materials*, vol. 265, p. 120 764, 2020.

[38] S. Rana, P. Subramani, R. Fangueiro, and A. G. Correia, "A review on smart self-sensing composite materials for civil engineering applications," *AIMS Materials Science*, vol. 3, no. 2, pp. 357–379, 2016.

[39] O. Starkova, S. Buschhorn, E. Mannov, K. Schulte, and A. Aniskevich, "Creep and recovery of epoxy/mwcnt nanocomposites," *Composites Part A: Applied Science and Manufacturing*, vol. 43, no. 8, pp. 1212–1218, 2012.

[40] D. Gao, M. Sturm, and Y. Mo, "Electrical resistance of carbon-nanofiber concrete," *Smart Materials and Structures*, vol. 18, no. 9, p. 095 039, 2009.

[41] L. Gao, T.-W. Chou, E. T. Thostenson, and Z. Zhang, "A comparative study of damage sensing in fiber composites using uniformly and non-uniformly dispersed carbon nanotubes," *Carbon*, vol. 48, no. 13, pp. 3788–3794, 2010.

[42] R. Howser, H. Dhonde, and Y. Mo, "Self-sensing of carbon nanofiber concrete columns subjected to reversed cyclic loading," *Smart materials and structures*, vol. 20, no. 8, p. 085 031, 2011.

[43] F. Azhari and N. Banthia, "Cement-based sensors with carbon fibers and carbon nanotubes for piezoresistive sensing," *Cement and Concrete Composites*, vol. 34, no. 7, pp. 866–873, 2012.

[44] G. Koo and T. Tallman, "Higher-order resistivity-strain relations for self-sensing nanocomposites subject to general deformations," *Composites Part B: Engineering*, vol. 190, p. 107 907, 2020.

[45] K. Aly, A. Li, and P. D. Bradford, "Compressive piezoresistive behavior of carbon nanotube sheets embedded in woven glass fiber reinforced composites," *Composites Part B: Engineering*, vol. 116, pp. 459–470, 2017.

[46] T. Tallman, S. Gungor, K. Wang, and C. E. Bakis, "Tactile imaging and distributed strain sensing in highly flexible carbon nanofiber/polyurethane nanocomposites," *Carbon*, vol. 95, pp. 485–493, 2015.

[47] F. Avilés, A. I. Oliva-Avilés, and M. Cen-Puc, "Piezoresistivity, strain, and damage self-sensing of polymer composites filled with carbon nanostructures," *Advanced Engineering Materials*, vol. 20, no. 7, p. 1 701 159, 2018.

[48] A. Todoroki, "Self-sensing composites and optimization of composite structures in japan," *International Journal of Aeronautical and Space Sciences*, vol. 11, no. 3, pp. 155–166, 2010.

[49] K. Ogi and Y. Takao, "Characterization of piezoresistance behavior in a cfrp unidirectional laminate," *Composites Science and Technology*, vol. 65, no. 2, pp. 231–239, 2005.

[50] X. Wang and D. Chung, "Continuous carbon fibre epoxy-matrix composite as a sensor of its own strain," *Smart materials and structures*, vol. 5, no. 6, p. 796, 1996.

[51] A. Todoroki and J. Yoshida, "Electrical resistance change of unidirectional cfrp due to applied load," *JSME International Journal Series A Solid Mechanics and Material Engineering*, vol. 47, no. 3, pp. 357–364, 2004.

[52] F. Nanni, G. Ruscito, G. Forte, and G. Gusmano, "Design, manufacture and testing of self-sensing carbon fibre–glass fibre reinforced polymer rods," *Smart materials and structures*, vol. 16, no. 6, p. 2368, 2007.

[53] C. Bakis, A. Nanni, J. Terosky, and S. Koehler, "Self-monitoring, pseudo-ductile, hybrid frp reinforcement rods for concrete applications," *Composites science and technology*, vol. 61, no. 6, pp. 815–823, 2001.

[54] N. Muto, H. Yanagida, T. Nakatsuji, M. Sugita, and Y. Ohtsuka, "Preventing fatal fractures in carbon-fiber–glass-fiber-reinforced plastic composites by monitoring change in electrical resistance," *Journal of the American Ceramic Society*, vol. 76, no. 4, pp. 875–879, 1993.

[55] A. Todoroki, M. Tanaka, and Y. Shimamura, "Measurement of orthotropic electric conductance of cfrp laminates and analysis of the effect on delamination monitoring with an electric resistance change method," *Composites Science and Technology*, vol. 62, no. 5, pp. 619–628, 2002.

[56] J. Abry, S. Bochard, A. Chateauminois, M. Salvia, and G. Giraud, "In situ detection of damage in cfrp laminates by electrical resistance measurements," *Composites Science and Technology*, vol. 59, no. 6, pp. 925–935, 1999.

[57] T. Swait, F. Jones, and S. Hayes, "A practical structural health monitoring system for carbon fibre reinforced composite based on electrical resistance," *Composites science and technology*, vol. 72, no. 13, pp. 1515–1523, 2012.

[58] R. P. Henderson and J. G. Webster, "An impedance camera for spatially specific measurements of the thorax," *IEEE Transactions on Biomedical Engineering*, no. 3, pp. 250–254, 1978.

[59] R. Harikumar, R. Prabu, and S. Raghavan, "Electrical impedance tomography (eit) and its medical applications: A review," *Int. J. Soft Comput. Eng*, vol. 3, no. 4, pp. 193–198, 2013.

[60] T. N. Tallman and D. J. Smyl, "Structural health and condition monitoring via electrical impedance tomography in self-sensing materials: A review," *Smart Materials and Structures*, vol. 29, no. 12, p. 123 001, 2020.

[61] M. Hallaji, A. Seppänen, and M. Pour-Ghaz, "Electrical impedance tomography-based sensing skin for quantitative imaging of damage in concrete," *Smart Materials and Structures*, vol. 23, no. 8, p. 085 001, 2014.

[62] J. G. Gonzalez, S. Gupta, and K. J. Loh, "Multifunctional cement composites enhanced with carbon nanotube thin film interfaces," *Proceedings of the IEEE*, vol. 104, no. 8, pp. 1547–1560, 2016. DOI: 10.1109/JPROC.2015.2503299.

[63] K. Loh, T.-C. Hou, J. Lynch, and N. Kotov, "Nanotube-based sensing skins for crack detection and impact monitoring of structures," in *Proceedings of the 6th International Workshop on Structural Health Monitoring, Stanford, CA, USA*, 2007, p. 16 851 692.

[64] T. N. Tallman, "Conductivity-based nanocomposite structural health monitoring via electrical impedance tomography.," PhD thesis, 2015.

[65] H. Hassan, F. Semperlotti, K.-W. Wang, and T. N. Tallman, "Enhanced imaging of piezoresistive nanocomposites through the incorporation of nonlocal conductivity changes in electrical impedance tomography," *Journal of Intelligent Material Systems and Structures*, vol. 29, no. 9, pp. 1850–1861, 2018.

[66] H. Hassan and T. N. Tallman, "Failure prediction in self-sensing nanocomposites via genetic algorithm-enabled piezoresistive inversion," *Structural Health Monitoring*, vol. 19, no. 3, pp. 765–780, 2020.

[67] T. N. Tallman, S. Gungor, K. Wang, and C. E. Bakis, "Damage detection via electrical impedance tomography in glass fiber/epoxy laminates with carbon black filler," *Structural Health Monitoring*, vol. 14, no. 1, pp. 100–109, 2015.

[68] A. Thomas, J. Kim, T. Tallman, and C. Bakis, "Damage detection in self-sensing composite tubes via electrical impedance tomography," *Composites Part B: Engineering*, vol. 177, p. 107 276, 2019.

[69] R. Schueler, S. P. Joshi, and K. Schulte, "Damage detection in cfrp by electrical conductivity mapping," *Composites science and technology*, vol. 61, no. 6, pp. 921–930, 2001.

[70] W. Lestari, B. Pinto, V. La Saponara, J. Yasui, and K. J. Loh, "Sensing uniaxial tensile damage in fiber-reinforced polymer composites using electrical resistance tomography," *Smart Materials and Structures*, vol. 25, no. 8, p. 085 016, 2016.

[71] A. Baltopoulos, N. Polydorides, L. Pambaguian, A. Vavouliotis, and V. Kostopoulos, "Damage identification in carbon fiber reinforced polymer plates using electrical resistance tomography mapping," *Journal of composite materials*, vol. 47, no. 26, pp. 3285–3301, 2013.

[72] S. Nonn, M. Schagerl, Y. Zhao, S. Gschossmann, and C. Kralovec, "Application of electrical impedance tomography to an anisotropic carbon fiber-reinforced polymer composite laminate for damage localization," *Composites Science and Technology*, vol. 160, pp. 231–236, 2018.

[73] J. Cagáň, J. Pelant, M. Kyncl, M. Kadlec, and L. Michalcová, "Damage detection in carbon fiber–reinforced polymer composite via electrical resistance tomography with gaussian anisotropic regularization," *Structural Health Monitoring*, vol. 18, no. 5-6, pp. 1698–1710, 2019.

[74] J. Cagáň and L. Michalcová, "Impact damage detection in cfrp composite via electrical resistance tomography by means of statistical processing," *Journal of Nondestructive Evaluation*, vol. 39, no. 2, pp. 1–12, 2020.

[75] A. Adler and W. R. Lionheart, "Uses and abuses of eidors: An extensible software base for eit," *Physiological measurement*, vol. 27, no. 5, S25, 2006.

[76] A. Adler, W. Lionheart, and N. Polydorides, *Eidors: Electrical impedance tomography and diffuse optical tomography reconstruction software*, 2015.

[77] J. Jauhiainen, M. Pour-Ghaz, T. Valkonen, and A. Seppänen, "Non-planar sensing skins for structural health monitoring based on electrical resistance tomography," *arXiv preprint arXiv:2012.04588*, 2020.

[78] T. Tallman and J. Hernandez, "The effect of error and regularization norms on strain and damage identification via electrical impedance tomography in piezoresistive nanocomposites," *NDT & E International*, vol. 91, pp. 156–163, 2017.

[79] D. Liu, V. Kolehmainen, S. Siltanen, and A. Seppänen, "A nonlinear approach to difference imaging in eit; assessment of the robustness in the presence of modelling errors," *Inverse Problems*, vol. 31, no. 3, p. 035 012, 2015.

[80] C. N. Herrera, M. F. Vallejo, J. L. Mueller, and R. G. Lima, "Direct 2-d reconstructions of conductivity and permittivity from eit data on a human chest," *IEEE transactions on medical imaging*, vol. 34, no. 1, pp. 267–274, 2014.

[81] J.-F. P. Abascal, S. R. Arridge, D. Atkinson, R. Horesh, L. Fabrizi, M. De Lucia, L. Horesh, R. H. Bayford, and D. S. Holder, "Use of anisotropic modelling in electrical impedance tomography; description of method and preliminary assessment of utility in imaging brain function in the adult human head," *Neuroimage*, vol. 43, no. 2, pp. 258–268, 2008.

[82] W. Lionheart, "Conformal uniqueness results in anisotropic electrical impedance imaging," *Inverse problems*, vol. 13, no. 1, p. 125, 1997.

[83] T. N. Tallman, F. Semperlotti, and K. Wang, "Enhanced delamination detection in multifunctional composites through nanofiller tailoring," *Journal of Intelligent Material Systems and Structures*, vol. 26, no. 18, pp. 2565–2576, 2015.

[84] H. Hassan and T. Tallman, "Damage sizing in self-sensing materials using a genetic algorithm-supplemented electrical impedance tomography formulation," in *Sensors and Smart Structures Technologies for Civil, Mechanical, and Aerospace Systems 2020*, International Society for Optics and Photonics, vol. 11379, 2020, 113790B.

A. DETAILED FORWARD PROBLEM

This appendix shall lay out the details of the finite element formulation of the forward problem as mentioned in chapter 3. Note, that indicial notation has been dropped while forming the matrices later in the chapter due to large number of subscripts and superscripts. The derivations here are referenced from [64].

A.1   Steady State Diffusion Weak Form and Discretization

$$-\frac{\partial j_i}{\partial x_i} = \frac{\partial}{\partial x_j}\sigma_{ij}\frac{\partial u}{\partial x_j} = f \tag{A.1}$$

In the given steady state diffusion equation for a domain, j_i is the current density vector, σ_{ij} is the conductivity tensor, u is the domain potential and f the internal current source. Based on the theory of conservation of charge, we assume that current entering at the electrodes is equal to the current leaving the electrodes. Also, we assume that no current flows through the boundaries where electrodes are not attached. These boundary conditions are given as follows.

$$\int_{E_l} \sigma_{ij}\frac{\partial u}{\partial x_i}n_j \; \mathrm{d}S_l = I_l \tag{A.2}$$

$$\sigma_{ij}\frac{\partial u}{\partial x_i}n_j = 0 \text{ off } \bigcup_{l=1}^{L} E_l \tag{A.3}$$

$$\sum_{l=1}^{L} I_l = 0 \tag{A.4}$$

In the equations above, n_j refers to the outward pointing normal and L is the total number of electrodes in the domain. The weak form is formulated by multiplying the diffusion equation by a weighting function ψ that satisfies the Dirichlet boundary conditions and then integrating the result of the domain.

$$\int_{\Omega} \psi\frac{\partial}{\partial x_j}\sigma_{ij}\frac{\partial u}{\partial x_j} \; \mathrm{d}\Omega = \int_{\Omega} \psi f \; \mathrm{d}\Omega \tag{A.5}$$

Due to the absence of internal current source, $f = 0$. With Green's second identity along with the vector identity, equation (A.5) can be rewritten as

$$\int_\Omega \frac{\partial}{\partial x_j} \psi \sigma_{ij} \frac{\partial u}{\partial x_i} \, \mathrm{d}\Omega - \int_\Omega \frac{\partial \psi}{\partial x_i} \sigma_{ij} \frac{\partial u}{\partial x_j} \, \mathrm{d}\Omega = 0 \tag{A.6}$$

On applying the divergence theorem,

$$\int_\Omega \frac{\partial \psi}{\partial x_i} \sigma_{ij} \frac{\partial u}{\partial x_j} \, \mathrm{d}\Omega = \int_{\partial\Omega} \psi \sigma_{ij} \frac{\partial u}{\partial x_i} n_j \, \mathrm{d}S = \int_\Gamma \sigma_{ij} \frac{\partial u}{\partial x_j} n_j \psi \, \mathrm{d}S \tag{A.7}$$

Here $\Gamma = \cup_l E_l$ is the union of the electrodes. Now, substituting (3.2) into (A.7) gives the following equation.

$$\int_\Omega \frac{\partial \psi}{\partial x_i} \sigma_{ij} \frac{\partial u}{\partial x_j} \, \mathrm{d}\Omega = \sum_{l=1}^{L} \int_{E_l} \frac{1}{z_l} (V_l - u) \psi \, \mathrm{d}S_l \tag{A.8}$$

The above equation is discretized by partitioning the domain Ω into disjoint subsets Ω_e so that it can be expressed as an assembly of these subsets as shown in (A.9). Here, $\sum_e (.)$ refers to the assembly of subsets.

$$\sum_e \int_{\omega_e} \frac{\partial \psi_e}{\partial x_i} \sigma_{ij} \frac{\partial u_e}{\partial x_j} \, \mathrm{d}\Omega_e = \sum_e \sum_{l=1}^{L} \int_{\partial\Omega_e} \frac{1}{z_l} (V_l - u_e) \psi_e \, \mathrm{d}S_e \tag{A.9}$$

u_e and ψ_e are expressed via interpolating functions. These formulations are given below.

$$u_e = \sum_{A=1}^{N} w^A d_e^A \tag{A.10}$$

$$\psi_e = \sum_{A=1}^{N} w^A c_e^A \tag{A.11}$$

Here, d_e^A is the solution to the forward problem at the Ath node of the eth element and c_e^A is the variation of the Ath node of the eth element. (A.10) is the interpolation of the nodal solutions over the eth element and summed over N nodes per element.

A.2 Finite Element Matrices

Substitute equation (A.10) and (A.11) into the left hand side of equation (A.9) to give the following.

$$\int_{\Omega_e} \frac{\partial \psi_e}{\partial x_i} \sigma_{ij} \frac{\partial u_e}{\partial x_j} \, d\Omega_e = \sum_{A=1}^{N} \sum_{B=1}^{N} c_e^A \int_{\Omega_e} \frac{\partial w^A}{\partial x_i} \sigma_{ij} \frac{\partial w^B}{\partial x_j} \, d\Omega_e d_e^B \tag{A.12}$$

Here c_e^A and d_e^A are constants, hence, they are pulled out of the integral. The interpolation functions are then defined on an isoparametric domain given as

$$x_i = \sum_{A=1}^{N} w^A(\zeta) x_i^A \tag{A.13}$$

where x_i^A is the i-coordinate of the Ath node. The isoparametric mapping is depicted for a 3D tetrahedral element in Figure (A.1).
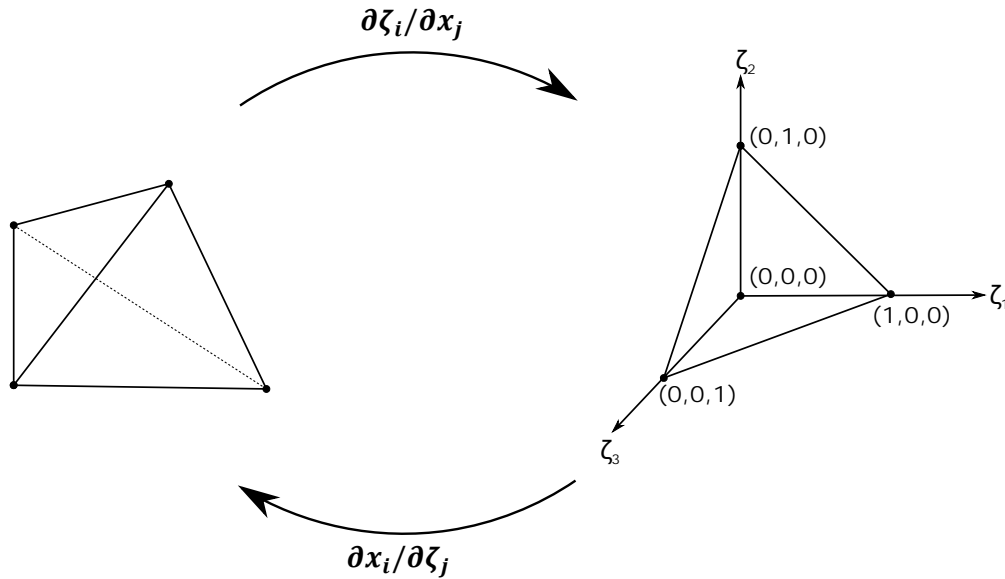
Figure A.1. A tetrahedral element shown to the left is mapped to an isoparametric domain shown to the right.

The chain rule of differentiation is employed to form the gradient of the interpolation functions

$$\frac{\partial w^A}{\partial x_i} = \frac{\partial w^A}{\partial \zeta_j} \frac{\partial \zeta_j}{\partial x_i} \tag{A.14}$$

Herein, $\partial \zeta_j / \partial x_i$ is the inverse of $\partial x_i / \partial \zeta_j$, formed by differentiating equation (A.13). Equation (A.12) can now be written as

$$\int_{\Omega_e} \frac{\partial \psi_e}{\partial x_i} \sigma_{ij} \frac{\partial u_e}{\partial x_j} \, d\Omega_e = \sum_{A=1}^{N} \sum_{B=1}^{N} c_e^A \int_{\Omega_e} \frac{\partial w^A}{\partial \zeta_k} \frac{\partial \zeta_k}{\partial x_i} \sigma_{ij} \frac{\partial w^B}{\partial \zeta_l} \frac{\partial \zeta_l}{\partial x_j} \, d\Omega_e d_e^B \tag{A.15}$$

Since we utilize an isoparametric domain, the integrals can be exactly calculated using the numerical quadrature with appropriately selected Lagrange polynomials. The linear tetrahedral elements used in this thesis are gives as $w^1 = \zeta_1$, $w^2 = \zeta_2$, $w^3 = \zeta_3$ and $w^4 = 1 - \zeta_1 - \zeta_2 - \zeta_3$. In order to express the integrals in the isoparametric domain, we must multiply it by $\det|\partial x_i / \partial \zeta_j|$.

$$\int_{\Omega_e} \frac{\partial \psi_e}{\partial x_i} \sigma_{ij} \frac{\partial u_e}{\partial x_j} \, d\Omega_e = \sum_{A=1}^{N} \sum_{B=1}^{N} c_e^A \int_{\Omega_{e\zeta}} \frac{\partial w^A}{\partial \zeta_k} \frac{\partial \zeta_k}{\partial x_i} \sigma_{ij} \frac{\partial w^B}{\partial \zeta_l} \frac{\partial \zeta_l}{\partial x_j} \det \left| \frac{\partial x_m}{\partial \zeta_n} \right| \, d\Omega_{e\zeta} d_e^B \tag{A.16}$$

Here, $\Omega_{e\zeta}$ is the integral of the eth element in the isoparametric domain. This equation is evaluated as a sum of weighted polynomials at quadrature points given as follows

$$\int_{\Omega_{e\zeta}} p(\zeta_l) \, d\Omega_{e\zeta} = \sum_{m}^{M} a_m p(\zeta_m) \tag{A.17}$$

In equation (A.17), the summation runs over the number of quadrature points and a_m is the mth weight. We can now form the elemental diffusion stiffness matrix.

$$\int_{\Omega_e} \frac{\partial \psi_e}{\partial x_i} \sigma_{ij} \frac{\partial u_e}{\partial x_j} \, d\Omega_e = \sum_{A=1}^{N} \sum_{B=1}^{N} c_e^A k_e^{AB} d_e^B = \begin{bmatrix} c_e^1 & c_e^2 & \dots & c_e^N \end{bmatrix} \boldsymbol{k}_e \begin{bmatrix} d_e^1 \\ d_e^2 \\ \vdots \\ d_e^N \end{bmatrix} \tag{A.18}$$

Here, k_e^{AB} is the local diffusion matrix of the eth element and is assembled into the global diffusion matrix $\boldsymbol{A}_M$. This local stiffness matrix for the eth tetrahedral element is explicitly stated as follows

$$
\boldsymbol{k}_e = \frac{1}{6}
\begin{bmatrix}
1 & 0 & 0 \\
0 & 1 & 0 \\
0 & 0 & 1 \\
-1 & -1 & -1
\end{bmatrix}
\begin{bmatrix}
x_1^e - x_4^e & x_2^e - x_4^e & x_3^e - x_4^e \\
y_1^e - y_4^e & y_2^e - y_4^e & y_3^e - y_4^e \\
z_1^e - z_4^e & z_2^e - z_4^e & z_3^e - z_4^e
\end{bmatrix}^{-1} \cdots
$$

$$
\cdots
\begin{bmatrix}
\sigma_{11} & \sigma_{12} & \sigma_{13} \\
\sigma_{21} & \sigma_{22} & \sigma_{23} \\
\sigma_{31} & \sigma_{32} & \sigma_{33}
\end{bmatrix}
\begin{bmatrix}
x_1^e - x_4^e & x_2^e - x_4^e & x_3^e - x_4^e \\
y_1^e - y_4^e & y_2^e - y_4^e & y_3^e - y_4^e \\
z_1^e - z_4^e & z_2^e - z_4^e & z_3^e - z_4^e
\end{bmatrix}^{-T} \cdots \qquad (A.19)
$$

$$
\cdots
\begin{bmatrix}
1 & 0 & 0 \\
0 & 1 & 0 \\
0 & 0 & 1 \\
-1 & -1 & -1
\end{bmatrix}^{T}
\det \left|
\begin{bmatrix}
x_1^e - x_4^e & x_2^e - x_4^e & x_3^e - x_4^e \\
y_1^e - y_4^e & y_2^e - y_4^e & y_3^e - y_4^e \\
z_1^e - z_4^e & z_2^e - z_4^e & z_3^e - z_4^e
\end{bmatrix}
\right|
$$

The volume of the tetrahedral element is given by

$$
V^e = \frac{1}{6}\det \left|
\begin{bmatrix}
x_1^e - x_4^e & x_2^e - x_4^e & x_3^e - x_4^e \\
y_1^e - y_4^e & y_2^e - y_4^e & y_3^e - y_4^e \\
z_1^e - z_4^e & z_2^e - z_4^e & z_3^e - z_4^e
\end{bmatrix}
\right| \qquad (A.20)
$$

Looking back at equation (A.9), $\boldsymbol{A}_Z$, $\boldsymbol{A}_W$ and $\boldsymbol{A}_D$ are formed on evaluating the right hand side of the equation.

$$
\sum_e \int_{\partial\Omega_e} \frac{1}{z_l}(V_l - u_e)\psi_e \, \mathrm{d}S_e = \sum_e \left(-\int_{\partial\Omega_e} \frac{1}{z_l}u_e\psi_e \, \mathrm{d}S_e + \int_{\partial\Omega_e} \frac{1}{z_l}V_l\psi_e \, \mathrm{d}S_e \right) \qquad (A.21)
$$

Note here that for $\boldsymbol{A}_Z$ and $\boldsymbol{A}_W$, we use interpolation functions that are one degree lower than the degree used for the domain discretization. Hence, in this case, we use $w^1 = \zeta_1$,

$w^2 = \zeta_2$ and $w^3 = 1 - \zeta_1 - \zeta_2$ for domain functions of $w^1 = \zeta_1$, $w^2 = \zeta_2$, $w^3 = \zeta_3$ and $w^4 = 1 - \zeta_1 - \zeta_2 - \zeta_3$. Further, we move the right hand side of equation (A.21) to the left hand side of equation (A.9) and substitute the expressions from (A.10) and (A.11).

For $\boldsymbol{A}_Z$, we use the first integral on the right hand side of (A.21) and consider the eth element of the lth electrode.

$$\int_{\partial\Omega_e} \frac{1}{z_l} u_e \psi_e \ dS_e = \sum_{A=1}^{N} \sum_{B=1}^{N} c_e^A \int_{\Omega_e} \frac{1}{z_l} w^A w^B \ dS_e \ d_e^B = \begin{bmatrix} c_e^1 & c_e^2 & \dots & c_e^N \end{bmatrix} \boldsymbol{A}_z^{el} \begin{bmatrix} d_e^1 \\ d_e^2 \\ \vdots \\ d_e^N \end{bmatrix} \quad \text{(A.22)}$$

The equation (A.22) can be evaluated to find $\boldsymbol{A}_Z^{el}$ matrix of the eth element of the lth electrode. In three-dimensional analysis, A_Z^{el} matrix of the eth linear tringle element of the lth electrode is

$$\begin{aligned}
\boldsymbol{A}_z^{el} &= \int_0^1 \int_0^{1-\zeta_1} \frac{2A^e}{z_l} \begin{bmatrix} \zeta_1^2 & \zeta_1\zeta_2 & \zeta_1(1-\zeta_1-\zeta_2) \\ \zeta_1\zeta_2 & \zeta_2^2 & \zeta_2(1-\zeta_1-\zeta_2) \\ \zeta_1(1-\zeta_1-\zeta_2) & \zeta_2(1-\zeta_1-\zeta_2) & (1-\zeta_1-\zeta_2)^2 \end{bmatrix} \ d\zeta_2 d\zeta_1 \\
&= \frac{A^e}{12z_l} \begin{bmatrix} 2 & 1 & 1 \\ 1 & 2 & 1 \\ 1 & 1 & 2 \end{bmatrix}
\end{aligned} \quad \text{(A.23)}$$

$\boldsymbol{A}_Z^{el}$ is formed for every element part of the electrode and then assembled to form the global $\boldsymbol{A}_Z$.

Matrix $\boldsymbol{A}_W$ relates the domain voltage to the electrode voltages. It is formed by evaluating the second integral on the right hand side of equation (A.21). Therefore, consider the eth element of the lth electrode.

$$-\int_{\partial\Omega_e} \frac{1}{z_l}V_l\psi_e \, \mathrm{d}S_e = -\sum_{A=1}^{N} c_e^A \int_{\Omega_e} \frac{1}{z_l}w^A \, \mathrm{d}S_e V_l = \begin{bmatrix} c_e^1 & c_e^2 & \dots & c_e^N \end{bmatrix} \boldsymbol{A}_W^{el} V_l \tag{A.24}$$

Electrode voltages, V_l are pulled out of the integral as they are assumed to be constant at an electrode. The column vector, $\boldsymbol{A}_W$ for the eth element of the lth electrode in three-dimensional analysis is given as

$$\begin{aligned} \boldsymbol{A}_W^{el} &= -\int_0^1 \int_0^{1-\zeta} \frac{2A^e}{z_l} \begin{bmatrix} \zeta_1 \\ \zeta_2 \\ 1 - \zeta_1 - \zeta_2 \end{bmatrix} \mathrm{d}\zeta_2 \mathrm{d}\zeta_1 \\ &= -\frac{A^e}{3z_l} \begin{bmatrix} 1 \\ 1 \\ 1 \end{bmatrix} \end{aligned} \tag{A.25}$$

Lastly, formulation of $\boldsymbol{A}_D$ is given below. The current through lth electrode is given as

$$I_l = \int_{E_l} \frac{1}{z_l}(V_l - u) \, \mathrm{d}S = \frac{1}{z_l}E_l V_l - \int_{E_l} \frac{1}{z_l}u \, \mathrm{d}S \tag{A.26}$$

On assuming a constant contact impedance and electrode voltage, the first quantity on the right hand side of equation (A.26) relates electrode current to the voltage by E_l/z_l, forming $\boldsymbol{A}_D$. The second term on the other hand can be related to equation (A.24) but with nodal solution instead of nodal variation. This accounts for the coupling of the domain voltage to the electrode voltage by $\boldsymbol{A}_W$.

B. DETAILED SENSITIVITY MATRIX FORMULATION

The sensitivity matrix calculation is quite similar to the formulation of the finite element stiffness matrix as seen in Appendix A. In here, we shall derive the exact form of the sensitivity matrix entries with respect to κ for linear tetrahedral elements utilized in this thesis. The sensitivity matrix formulation with respect to in-plane ($\boldsymbol{J}_\parallel$) and through-thickness ($\boldsymbol{J}_\perp$) conductivity is skipped here since these Jacobians are essentially formed from voltage vectors obtained through multiple runs of the forward problem.

B.1 Evaluation of Sensitivity Matrix Entries

The equation from Chapter 3 for the Jacobian with respect to the scalar multiple of the conductivity tensor is restated as shown below, with change of index from MN to QR. This was done to avoid using the same indices used to sum over the number of nodes per element.

$$J^\kappa_{QR\,e} = -\int_{\Omega_e} \frac{\partial u^Q}{\partial x_i} \bar{\sigma}^e_{ij} \frac{\partial \bar{u}^R}{\partial x_i} \, \mathrm{d}\Omega_e \tag{B.1}$$

We shall start by substituting equation (A.10) into equation (B.1).

$$J^\kappa_{QR\,e} = -\int_{\Omega_e} \frac{\partial u^Q}{\partial x_i} \bar{\sigma}^e_{ij} \frac{\partial \bar{u}^R}{\partial x_i} \, \mathrm{d}\Omega_e = -\sum_{A=1}^{N}\sum_{B=1}^{N} d^{AQ}_e \int_{\Omega_e} \frac{\partial w^A}{\partial x_i} \bar{\sigma}_{ij} \frac{\partial w^B}{\partial x_j} \, \mathrm{d}\Omega_e \bar{d}^{BR}_e \tag{B.2}$$

Here, d^{AQ}_e refers to the Ath nodal solution of the eth element due to the Qth injection, and $\bar{d}^{BR}_e$ refers to the Bth nodal solution of the eth solution of the eth element due to a unit current injection by the Rth electrode measurement pair. The gradients of the interpolation function can now be evaluated via the chain rule. On integration in the isoparametric domain, we get the following equation.

$$-\int_{\Omega_e} \frac{\partial u^Q}{\partial x_i} \bar{\sigma}^e_{ij} \frac{\partial \bar{u}^R}{\partial x_i} \, \mathrm{d}\Omega_e = -\sum_{A=1}^{N}\sum_{B=1}^{N} d^{AQ}_e \int_{\Omega_e} \frac{\partial w^A}{\partial \zeta_k} \frac{\partial \zeta_k}{\partial x_i} \bar{\sigma}_{ij} \frac{\partial w^B}{\partial \zeta_l} \frac{\partial \zeta_l}{\partial x_j} \det\left|\frac{\partial x_m}{\partial \zeta_n}\right| \, \mathrm{d}\Omega_e \bar{d}^{BR}_e \tag{B.3}$$

Expressing the summations through linear algebra, we get

$$-\int_{\Omega_e} \frac{\partial u^Q}{\partial x_i} \bar{\sigma}_{ij}^e \frac{\partial \bar{u}^R}{\partial x_i} \, d\Omega_e = \sum_{A=1}^{N} \sum_{B=1}^{N} d_e^{AQ} j_e^{AB} \bar{d}_e^{BR} = \begin{bmatrix} d_e^{1Q} & d_e^{2Q} & \dots & d_e^{NQ} \end{bmatrix} \boldsymbol{j}_e \begin{bmatrix} \bar{d}_e^{1R} \\ \bar{d}_e^{2R} \\ \vdots \\ \bar{d}_e^{NR} \end{bmatrix} \qquad (B.4)$$

$\boldsymbol{j}_e$ for tetrahedral element is written out as

$$\boldsymbol{j}_e = -\frac{1}{6} \begin{bmatrix} 1 & 0 & 0 \\ 0 & 1 & 0 \\ 0 & 0 & 1 \\ -1 & -1 & -1 \end{bmatrix} \begin{bmatrix} x_1^e - x_4^e & x_2^e - x_4^e & x_3^e - x_4^e \\ y_1^e - y_4^e & y_2^e - y_4^e & y_3^e - y_4^e \\ z_1^e - z_4^e & z_2^e - z_4^e & z_3^e - z_4^e \end{bmatrix}^{-1} \dots$$

$$\dots \begin{bmatrix} \bar{\sigma}_{11} & \bar{\sigma}_{12} & \bar{\sigma}_{13} \\ \bar{\sigma}_{21} & \bar{\sigma}_{22} & \bar{\sigma}_{23} \\ \bar{\sigma}_{31} & \bar{\sigma}_{32} & \bar{\sigma}_{33} \end{bmatrix} \begin{bmatrix} x_1^e - x_4^e & x_2^e - x_4^e & x_3^e - x_4^e \\ y_1^e - y_4^e & y_2^e - y_4^e & y_3^e - y_4^e \\ z_1^e - z_4^e & z_2^e - z_4^e & z_3^e - z_4^e \end{bmatrix}^{-T} \dots \qquad (B.5)$$

$$\dots \begin{bmatrix} 1 & 0 & 0 \\ 0 & 1 & 0 \\ 0 & 0 & 1 \\ -1 & -1 & -1 \end{bmatrix}^T \det \left(\begin{bmatrix} x_1^e - x_4^e & x_2^e - x_4^e & x_3^e - x_4^e \\ y_1^e - y_4^e & y_2^e - y_4^e & y_3^e - y_4^e \\ z_1^e - z_4^e & z_2^e - z_4^e & z_3^e - z_4^e \end{bmatrix} \right)$$

Note, that unlike the diffusion stiffness matrix formulation seen in the previous section, each entry calculated for the sensitivity matrix here is a scalar. This is because the nodal solution d_e^{AQ} and $\bar{d}_e^{BR}$ are known vectors, leading to scalar values. In case of the diffusion stiffness matrices, the contracting vectors were either variations to be minimized or solutions to be recovered.